Diverse clonal fates emerge upon drug treatment of homogeneous cancer cells

Yogesh Goyal[1,2,3,4,*], Gianna T. Busch[4], Maalavika Pillai[1,2,3], Jingxin Li[7], Ryan H. Boe[7], Emanuelle I. Grody[1,2,3], Manoj Chelvanambi[12], Ian P. Dardani[4], Benjamin Emert[5], Nicholas Bodkin[1,2,3], Jonas Braun[1,2,3], Dylan Fingerman[6], Amanpreet Kaur[5], Naveen Jain[7], Pavithran T. Ravindran[7], Ian A. Mellis[4,5], Karun Kiani[7], Gretchen M. Alicea[8,9], Mitchell E. Fane[8,9], Syeda Subia Ahmed[1,2,3], Haiyin Li[6], Yeqing Chen[6], Cedric Chai[1,2,3,10], Jessica Kaster[6], Russell G. Witt[12], Rossana Lazcano[12,13], Davis R. Ingram[12,13], Sarah B. Johnson[12], Khalida Wani[12], Margaret C. Dunagin[4,11], Alexander J. Lazar[12,14], Ashani T. Weeraratna[8,9], Jennifer A. Wargo[12], Meenhard Herlyn[6], and Arjun Raj[4,11,*]

[1]Department of Cell and Developmental Biology, Feinberg School of Medicine, Northwestern University, Chicago, IL, USA
[2]Center for Synthetic Biology, Northwestern University, Chicago, IL, USA
[3]Robert H. Lurie Comprehensive Cancer Center, Northwestern University Feinberg School of Medicine, Chicago, IL, USA
[4]Department of Bioengineering, School of Engineering and Applied Sciences, University of Pennsylvania, Philadelphia, PA, USA
[5]Genomics and Computational Biology Graduate Group, Perelman School of Medicine, University of Pennsylvania, Philadelphia, PA, USA
[6]The Wistar Institute, Philadelphia, PA, USA
[7]Genetics and Epigenetics, Cell and Molecular Biology Graduate Group, Perelman School of Medicine, University of Pennsylvania, Philadelphia, PA, USA
[8]Department of Biochemistry and Molecular Biology, Johns Hopkins School of Public Health, Baltimore, MD, USA
[9]Department of Oncology, Sidney Kimmel Cancer Center, Johns Hopkins School of Medicine, Baltimore MD, USA
[10]Center for Reproductive Science, Northwestern University, Chicago, IL, USA
[11]Department of Genetics, Perelman School of Medicine, University of Pennsylvania, Philadelphia, PA, USA
[12]Department of Genomic Medicine, Division of Cancer Medicine, The University of Texas MD Anderson Cancer Center, Houston, TX, USA
[13]Department of Translational Molecular Pathology, The University of Texas MD Anderson Cancer Center, Houston, TX, USA
[14]Department of Pathology, The University of Texas MD Anderson Cancer Center, Houston, TX, USA

*Authors for correspondence: yogesh.goyal@northwestern.edu and arjunrajlab@gmail.com

Abstract

Even amongst genetically identical cancer cells, therapy resistance often only emerges from a small subset of those cells[1–7]. Molecular differences in rare individual cells in the initial population allow certain cells to become therapy resistant[7–9]; however, comparatively little is known about variability in the resistant outcomes themselves. Here, we develop and apply FateMap, a framework that combines DNA barcoding with single-cell RNA sequencing, to reveal the fates of hundreds of thousands of clones exposed to anti-cancer therapies. We show that resistant clones emerging from single-cell-derived cancer cells adopt molecularly, morphologically, and functionally distinct resistant types. These different resistant types are largely predetermined by molecular differences between cells before drug addition and not by extrinsic factors. Changes in dose and kind of drug can switch the resistant type of an initial cell, resulting in the generation and elimination of certain resistant types. Patient samples show evidence for the existence of these resistant types in a clinical context. Diversity in resistant types was observed across several single-cell-derived cancer cell lines and types treated with a variety of drugs. Cell resistant type diversity as a result of variability in intrinsic cell states may be a generic feature of response to external cues.

Introduction

Individual cells respond to signals and stresses differently, often due to intrinsic, non-genetic differences[5,6,10–15]. Advances in single-cell barcoding enable tracking molecular state changes after signals and stresses over time[8,16–27], yet less attention has been paid to characterizing variability in the outcomes themselves. Typically, the implicit assumption is that outcomes are binary: induced or not induced, proliferative or nonproliferative, alive or dead. It is possible, however, that there is a far richer set of outcomes.

Therapy resistance in cancer illustrates variable responses to stress. Anti-cancer drugs often kill most cells, but a small, resistant subpopulation often remains, preventing cures. Recent studies have identified these subpopulations (marked by slow fluctuations in gene expression[1–4,7,9,28,29]) within even single-cell-derived (clonal) cancer populations. Upon drug exposure, clones from these populations survive and proliferate to form resistant colonies. Resistant cells are assumed to be relatively uniform in molecular profile and behavior, but it is unclear if the population's clonal structure results in variability. While a variety of resistance mechanisms have been documented[2,9,30–32] and differences in proliferative capacity suggest heterogeneity between resistant clones[8,20,22], it is unclear if diverse resistant cell types can arise from a homogeneous initial population.

We developed FateMap, a framework combining single-cell RNA sequencing, DNA barcoding, and computational analysis, to follow the fates of thousands of individual cancer cell clones as they acquire resistance. Even homogeneous cells grown in identical conditions gave rise to molecularly and functionally diverse resistant types. These types were predetermined by the intrinsic differences between them preceding drug exposure. Transcriptional and functional diversification of resistant types were consistent across different cancers and therapies.

Results

Diverse fates emerge upon drug treatment

We wondered whether the resistant cells that emerged from the treatment of single-cell-derived cancer cells adopted distinct fates. We focused on BRAF^{V600E}-mutated melanoma, where treatment of single-cell-derived cells with the targeted therapy vemurafenib lead to survival of rare (1:1,000 or less) cells, which proliferate to form resistant colonies (Figure 1A; Supplementary video 1). We performed single-cell RNA sequencing on a mixture of all the resistant colonies from a single tissue culture dish, finding that resistant types exhibited extensive diversity in their gene expression profiles (Figure 1B; Supplementary Figure 1). Some resistant cells expressed canonical resistance markers (e.g. *AXL, SERPINE1*)[1,3,8], but several other subpopulations expressed their own distinct sets of marker genes.

They expressed multiple markers reminiscent of particular cell types, including smooth muscle (e.g. *ACTA2, ACTG2, MYOCD*), neural crest (e.g. *NGFR, S100B, GAS7*), adhesive (e.g. *VCAM1, PKDCC, ITGA8*), melanocytic (e.g. *MLANA, SOX10, MITF*), or type-1 interferon signaling-enriched (e.g. *IFIT2, DDX58, OASL*) (Figure 1B,C; Supplementary Figure 1). Thus, diverse resistant cell states can emerge from single-cell-derived cancer cells upon treatment with targeted therapy. Resistant cells were more transcriptionally diverse than drug-naive, non-resistant cells[33] (Extended Data Figure 1A-G; Supplementary Discussion).

Resistant cells grow out as separate clones from individual cells amidst the initial drug-naive population (Supplementary video 1). Do all cells of a clone share a single resistant type, or comprise many types (Figure 1D-F)? Within-clone diversity implies that resistant cells can switch between subtypes. Between-clone diversity implies that resistant clones are transcriptionally stable. To determine both the transcriptional profile and clonal origin of each cell simultaneously, we developed FateMap, a method that uses transcribed DNA barcodes (encoded in the 3' untranslated region of gene encoding GFP) to identify clones from thousands of resistant cells at once (Figure 1D). First, lentiviral barcodes integrate into the DNA of therapy-naive cells. With a large barcode library complexity (~59 million unique barcodes, see Methods) and small multiplicity of infection, many thousands of cells could be uniquely barcoded and enriched by sorting. We exposed barcoded cells to vemurafenib, collected resistant populations, performed single-cell RNA sequencing, and extracted the FateMap clone barcode for each cell by selectively amplifying and sequencing the cDNA library in a way that linked the clone barcode and cell identifier (see Methods) (Figure 1E; Supplementary Figure 2; Supplementary Discussion).

Cells from individual resistant clones fell predominantly within constrained regions of transcriptional space, showing that variability was primarily between clones (Figure 1F,G). One large resistant clone was enriched for genes expressed in smooth muscle (e.g. *ACTA2, MYOCD*) while another, smaller clone, was enriched for genes expressed in neural crest cells (e.g. *NGFR, S100B*) (Figure 1G, Supplementary Figure 3). Other clones were enriched for canonical resistance markers (e.g. *AXL, SERPINE1*) (Supplementary Figure 1). Another subpopulation expressed the melanocyte genes *SOX10* and *MLANA*, predominantly consisting of single barcoded cells ("singletons") that were largely non-proliferative (Figure 1G, Supplementary Figure 3) (98.6% of all clones within clusters 0 and 3 were singletons). Barcode silencing was minimal and consistent between different resistant types (Supplementary Figure 1 and 2). Occasionally, cells in a clone belonged to two non-neighboring clusters, e.g., cluster 15 and 6 for three clones marked by *VCAM1* and *APOE*, respectively (Supplementary Figure 1).

Drug-naive cells also showed transcriptional constraint after 9 days in culture (~4 divisions) butwill over time span the entire transcriptomic space[7], whereas therapy-resistant clones remained constrained after months in drug (Extended Data Figure 1 A-C).

To quantify transcriptional homogeneity within a clone, we performed a dominant cluster analysis, showing that clones largely consisted of transcriptionally similar cells regardless of clustering resolution (Figure 1H, Supplementary Figure 3). Other statistical metrics[27,33,34] supported this conclusion (Supplementary Figure 3 and 4; Supplementary Discussion).

We corroborated these results by performing multiplex single molecule RNA fluorescence in situ hybridization (RNA FISH) for a subset of genes (*ACTA2, NGFR, BGN*) that belonged to distinct clusters (Figure 1C; Supplementary Figure 2) on a large plate containing several resistant clones. We verified that the selected markers expressed only in distinct resistant clones (Figure 1I; Supplementary Figure 5).

To show that there was not a genetic basis for the observed diversity of resistant types, we performed whole genome sequencing on both naive and resistant clones, finding no evidence of recurrent driver mutations (Extended Data Figure 2). We also grew out resistant colonies from the original WM989 A6-G3 cell line as well as two subclones, WM989 A6-G3 A10 and WM989 A6-G3 A11, and performed large-scale single molecule RNA FISH to demonstrate that resistant types emerged with the same frequency despite having different background mutations (Supplementary Figure 6).

Resistant types are functionally diverse

We wondered whether transcriptionally distinct resistant clones had different phenotypic properties. To measure differences in proliferation, we counted the number of cells per clone for different resistant types (Figure 2A,B; Supplementary Figure 6). Distinct resistant types had different proliferative capacities. Some types, e.g. those marked by *ACTA2, AXL,* and *VCAM1,* formed large colonies (Figure 2B), while those marked by *NGFR* (cluster 7) formed small colonies and singletons (Figure 2B).

Next, we asked whether different resistant clones exhibited distinct morphologies. We performed brightfield imaging of resistant colonies on the plate and identified several distinct morphologies (Figure 2C), including colonies with cells that appeared epithelial (type 1), cells that grew slower and were more transparent (type 2), cells that grew on top of each other (fate type 3), and elongated cells (type 4). For a subset of the types, we were able to isolate the colony and perform multiple cycles of growth and replating in the presence of vemurafenib; these colonies retained their morphology (Figure 2D) (some colonies did not survive the replating process). Furthermore, a systematic longitudinal analysis of several dozen isolated and expanded resistant colonies in vemurafenib revealed that colonies retain their phenotypes, such as morphology and transcriptional makeup, over 1-2 months (Extended Data Figure 3A-G) (18 for initial time points, 27 for late time points (4-6 weeks), and 13 paired initial-late time point colonies).

We then tested whether resistant colonies differed in invasive potential using a spheroid assay (see Methods). We manually isolated 64 therapy resistant colonies from multiple parallel experiments and expanded them for months. We formed 3D aggregates (spheroids) from a subset of resistant colonies with sufficient cell numbers, embedded them in a collagen matrix, and measured their invasiveness by measuring the area under the invading boundary (red) relative to that of the embedded spheroid core (blue) (Figure 2E,F). We found that different resistant clones had dramatically different invasion areas in the collagen matrix (some colonies were unable to aggregate into spheroids) (Figure 2E,F).

We then connected this variation in morphology and invasiveness to specific transcriptional profiles (Figure 2D). We performed bulk RNA sequencing of manually isolated colonies with known morphology and invasive potential. We identified genes differentially expressed between morphology types from bulk RNA sequencing and used these gene sets to map morphologies to single-cell clusters from Fatemap (see Methods) (Figure 2G). For example, we found the fate type 2 and fate type 3 morphology from Figure 2C corresponded to gene expression signatures most similar to the *NGFR*-high cluster (cluster 7) and *VCAM1*-high cluster (cluster 15) (Figure 2G; Supplementary Table 4). Similarly, several differentially expressed genes between slow and fast invading resistant colonies were connected to specific transcriptional clusters from FateMap (Extended Data Figure 3H). The fastest invading resistant colonies were enriched for expression of genes that marked cluster 8, including *ACTA2, TAGLN* and *EDN1*. Therefore, gene expression differences between clones corresponded to functional differences in proliferation, morphology, and invasiveness.

Diverse resistant types occur across cancers

We looked for diversity of resistant types in other cancer cell lines (Supplementary Discussion). Another single-cell-derived patient-derived melanoma cell line ($BRAF^{V600E}$ WM983B E9-C6) also showed morphological and proliferative differences between resistant clones upon vemurafenib treatment (Extended Data Figure 4A). FateMap revealed many of the same transcriptional signatures and proliferative differences seen in WM989 A6-G3 cells (Extended Data Figure 4B-F). We performed FateMap analysis on two NRAS mutant melanoma lines ($NRAS^{Q61K}$ WM3451 P2G7 and $NRAS^{Q61K}$ WM3623 P4E7) and again found a diversity of types in resistant clones to be a property of melanoma cell lines regardless of driver mutation (Extended Data Figure 4H-L and 5A-E). Furthermore, FateMap revealed extensive transcriptional diversity in clones of expanded primary human melanocytes (Extended Data Figure 6) (also observed in[1]), suggesting transcriptional diversity may be a general feature of the melanocyte lineage. FateMap applied to the triple negative breast cancer line MDA-MB-231-D4 treated with chemotherapy drug paclitaxel[7] also showed resistant clones occupying constrained regions of transcriptional space, albeit with less overall heterogeneity than in melanoma (Extended Data Figure 7).

Resistant types emerge in patients

We wondered whether these resistant types also arose in patients, in which the microenvironment (including immune system) and spatial context are factors. We obtained tissue samples of tumors from four patients who had relapsed subsequent to treatment with targeted therapy. (For two of them, we also had matching tumor samples from the patients before they underwent therapy). Multiple punch biopsies were taken from the tumor (Figure 3A). We used GeoMx spatial transcriptomic profiling, in which multiple regions of interest consisting of anywhere between 73 and 1,390 cells were selected from within each punch biopsy and profiled by RNA sequencing (93 regions across all samples, Supplementary Figure 7) (Figure 3). We found extensive variability in the expression of key resistant type markers across resistant tumor patches, suggesting that different areas of the same tumors within the same patient may harbor different proportions of the resistant types identified by FateMap (Figure 3B). There were multiple examples of adjacent regions from the same resistant tumor showing differential expression of markers from different resistant types. For example, within a single punch biopsy from patient 163, two regions showed high *MLANA/SOX10* expression while a third region showed high *ACTA2* expression (Figure 3B). Reassuringly, we found many patterns of coexpression (e.g. *ACTA2* and *ACTG2*, both from the smooth muscle resistant type identified by FateMap), further corroborating the existence of coherent resistant types in resistant tumors (Supplementary Figure 11). We found similar pre-existing variability in adjacent regions in patient-matched tumor samples prior to treatment with targeted therapy, suggesting some degree of pre-existing heterogeneity (Figure 3B, right side, and Supplementary Figure 8). To look for evidence for clonal structure of expression heterogeneity in the patient data, we used spatial proximity as an approximation of relatedness (Methods, Supplementary Figure 9), estimating that the degree of imbalance required to match that observed was on the order of 20%. Our findings suggested that the regions we captured were somewhat imbalanced but not completely clonal, which was expected given the relatively large sizes of the regions (Supplementary Figure 9). An analysis across other datasets showed further concordance with our FateMap results (Supplementary Figure 10). Furthermore, we found heterogeneity in immune infiltration after targeted therapy. For example, in a single punch biopsy, one region had high expression of macrophage marker *CD68* and while nearby regions had low expression of *CD68* but high levels of *CD8A* (Supplementary Figure 8). Together, these results provided strong evidence for the existence of diverse resistant types in patient samples.

We also looked for resistant types in xenograft models by injecting WM989 A6-G3 5a3[35] subcutaneously into mice, applying targeted therapy treatment, harvesting the resistant tumors, and measuring marker expression (Supplementary Figure 11). Large-scale scans of tumor tissue sections showed that markers for the various resistant types were present in distinct regions of the tumor sections (Supplementary Figures 11-13).

Resistant fates predetermined by initial conditions

We wondered whether the transcriptional and phenotypic variability in therapy resistant clones was the result of intrinsic differences in the molecular expression states of cells preceding drug exposure. Alternatively, the resistant types may be determined extrinsically, e.g. by the location and immediate neighbors of cells[33]. An “identical twin” analysis combined with Fatemap enabled us to distinguish between these possibilities.

Briefly, upon uniquely barcoding cells, we allowed them to divide for a few divisions and then separated the population into two equal split populations A and B such that most barcoded clones (>90%) were present in each group as “twins” (Figure 4A). We then applied vemurafenib and performed FateMap on both split populations. If the resistant type of a cell were intrinsically determined, then its twin would share the same type (assuming that the intrinsic potential has enough memory to be maintained over at least a few cell divisions[1,3,7,8]. Pure barcode sequencing of genomic DNA (gDNA) confirmed a strong overlap (significantly larger than random) in barcodes between the populations, demonstrating that resistance potential in general was intrinsically determined (we added specific amounts of known barcoded cells as standards (see Methods) to enable conversion of sequencing reads to the cell numbers) (Figure 4B,C). Mouse xenograft studies showed a lower but still statistically significant overlap as well (Supplementary Figure 14).

We next asked whether the specific type that a resistant clone adopted was similarly predetermined by the initial state of the pre-resistant cell as opposed to external factors. That is, did twins separated into the two split populations (thus randomizing the position in the plate and neighboring cells) adopt similar or distinct transcriptional profiles after drug treatment? An initial inspection of the clones painted on the UMAP projections suggested that twins surviving therapy largely end up in the same regions of the UMAP (Figure 4D and Supplementary Figure 6G-J) and were more similar than non-twin clones belonging to similar type clusters (Figure 4E).

To compare single-cell transcriptional profiles of clones across split populations, we formulated a metric we called the “mixing coefficient” (see Methods), which provides a pairwise comparison of transcriptional similarity between any two clones in principal component space (notably, it is independent of any particular cluster designation). For each pair of clones (twin or non-twin), we measured, for each cell, the number of nearby neighbor cells (from the pair of clones) that were either from the same clone (self-neighbor) or the pair clone. The mixing coefficient was the averaged fraction of self-neighbors across all cells from the clone pair divided by the averaged fraction of non-self neighbors. A mixing coefficient of 1 signifies a high degree of shared transcriptional similarity between the pair, while a mixing coefficient of 0 implies that the two clones are transcriptionally separated in the principal component space (see Methods). Non-twin clone pairs had low mixing coefficients both within or across the two split populations, but twin clone pairs exhibited high mixing coefficients (Figure 4F-H and Supplementary Figure 14). These results show that the adoption of distinct transcriptional and phenotypic types was determined by the intrinsic molecular state of the cells preceding drug exposure, and environmental factors had little to no effect on the type outcomes. Similar results in primary melanocytes and untreated WM989 A6-G3 melanoma cells showed that the intrinsic states of these cells persisted despite a change in a cell’s environment (Extended Data Figure 1H and Extended Data Figure 6). Intrinsic predetermination of resistant type also occurred in three other melanoma cell lines (WM983B A6-G3, WM3451 P2G7 and WM3623 P4E7), one primary melanocyte sample, and the breast cancer cell line tested earlier (MDA-MB-231-D4) (Extended Data Figure 4,5,7). The effects were less pronounced in the MDA-MB-231-D4 line (Extended Data Figure 7).

Changing drug dose causes fate switching

Drug resistance depends heavily on the concentration of drug used. We wondered how the ensemble of resistant types would change if we used a different drug concentration, so we performed FateMap across two split populations, each treated with a different concentration of drug.

We compared 100 nM vemurafenib to our standard dose of 1 µM (Supplementary Figure 15), which led to ~2.5-fold more resistant colonies than at the high dose (Figure 5A; Supplementary video 1,2). (Resistant tumors grew comparatively faster in the low dose in mice; Supplementary Figure 13A and Supplementary Figure 15). This increase could have resulted from 1) new resistant clones in addition to those that survive high dose, 2) a completely distinct set of clones becoming resistant, or 3) the same set of clones from high dose becoming resistant, but additional divisions of those clones (Figure 5B). FateMap could distinguish between these possibilities by splitting the population after barcoding and putting one set of twins in low dose and the other in high dose. gDNA barcode sequencing and imaging analysis showed many barcodes arising only in low dose, indicating that additional new clones became resistant in the low dose (fold change 2.15 and 2.55, respectively) (Figure 5A and Supplementary Figure 15). Barcode overlap between two low dose arms also showed intrinsic predetermination (Supplementary Figure 15).

We next asked how the diversity of resistant clones changed between low and high doses of drug. Despite the extensive change in the frequency of resistance between low and high dose, many of the transcriptional types were the same between the two doses (Figure 5C-F and Supplementary Figure 15). However, there were many differences as well. Particularly, the *NGFR*-high cells (cluster 9) were largely missing from the low dose resistant population of cells. Additionally, while *MLANA*-high cells (clusters 5,6) were present at both doses, they were in non-overlapping clusters (Figure 5C-F).

What was the fate of the *NGFR*-high resistant cells at low dose? We collected the barcoded clones corresponding to the *NGFR*-high cells in the high dose (cluster 9) and looked for their corresponding twins in the low dose (Figure 5G), finding 46 such barcodes (25.3% of all barcodes in cluster 9) (Figure 5G). Most of these clones (38/46) adopted types within the *MLANA*-high cluster 6 (fate switch 1) (Figure 5H). The remaining twins appeared to adopt a different, albeit less transcriptionally constrained, type (fate type switch 2) (Figure 5H). Several genes were differentially expressed in pairwise comparisons across the type switches (149 and 216 genes for switch 1 and 2, respectively) (Supplementary Figure 15 and Supplementary Table 8).

Comparing the 38/46 clones with the remaining 8/46 clones within the high dose, 70 genes were differentially expressed at high dose (Supplementary Figure 15), suggesting that subtle differences between naive cells that appeared to adopt the same *NGFR*-high type at high dose could lead to more obvious fate differences at low dose.

For the *MLANA*-high resistant type clusters, the percentage of non-singletons within the type increased strongly at low dose (4.66% in high dose to 21.6% in low dose) (Figure 5F and Supplementary Figure 15), indicating phenotypic differences in the type of resistant cells between high and low dose.

Metronomic therapy, in which therapy is given in discontinuous intervals, has been proposed as a means by which to decrease therapy resistant tumor burden with mixed results[36,37]. We measured the number and type of resistant clones in continuous vs. discontinuous dosing regimens with FateMap (Extended Data Figure 8). Discontinuous dosing resulted in overall greater numbers of resistant cells, both from new clones and increased growth of existing clones. Clones that formed the singleton *MLANA*-high resistant cells in continuous dosing grew to larger colony sizes in discontinuous dosing, confirmed by time-lapse imaging (Supplementary Figure 16).

Drug conditions affect ensemble of fates

We wondered if different MAPK inhibitors would have differential effects on resistant types (Supplementary Discussion). We performed FateMap on a population split between exposure to BRAF-V600E inhibitor vemurafenib (1 µM) and MEK inhibitor trametinib (5 nM). While many resistant cells from each drug had similar transcriptional profiles (Extended Data Figure 9A,B), we saw a depletion of *MLANA*-high cells (cluster 3) in trametinib compared to vemurafenib (Extended Data Figure 9A,F). The number of singletons were significantly higher in vemurafenib compared to trametinib (Extended Data Figure 9C), confirmed by imaging (Extended Data Figure 9D-E; Supplementary video 1,3). Most of the vemurafenib cluster 3 clones did not have corresponding twins in trametinib (Extended Data Figure 9G), suggesting that those cells were actually killed by trametinib as opposed to being converted to a different resistant type (Extended Data Figure 9H-I,O).

The *NGFR*-high cluster 4 was more populated in cells treated with trametinib compared to vemurafenib (Extended Data Figure 9B,J-K,P-Q). Twins of trametinib-treated *NGFR*-high cells adopted either the same type (*NGFR*-high) or in some cases the *MLANA*-high type in vemurafenib

(Extended Data Figure 9L-N). Additionally, resistant cells from dual treatment were transcriptionally indistinguishable from trametinib alone (Extended Data Figure 9R-S), suggesting that for the doses tested, trametinib dominated type outcomes.

We also tested the inhibition of the histone methyltransferase DOT1L for its effects on resistant types. We previously showed that pretreatment with pinometostat, a DOT1L inhibitor, increased resistance[35]; FateMap applied to pinometostat-pretreated cells showed that this increase arose from new clones becoming resistant but adopting largely the same types as they did normally (Extended Data Figure 10; Supplementary Discussion).

Discussion

FateMap revealed extensive variability in the outcome of cells after an external cue, in this case between resistant cancer cells after treatment with targeted therapies. These outcomes are largely predetermined by molecular differences in the initial state of cells, some of which have been elucidated[8]. The rich mapping between the initial molecular states of cells and their outcome is strongly dependent on the external cue — different doses and drugs dictate which cells adopt what types, and hence must be specified as part of the mapping.

A central challenge for the field is to define biologically meaningful “clusters” based on which molecular differences are important vs. inconsequential for relevant biological behaviors. Methods like ClonoCluster[38] that combine clonal information with transcriptomics may help resolve such issues.

The two factors underlying cell type determination in response to a cue are the memory of the initial state and the influence of extrinsic factors. Here, memory of the state means that twins largely adopted the same types, indicating type was largely intrinsically determined. By contrast, a similar analysis on cardiac differentiation[33] revealed that cell type was largely determined by extrinsic factors. It is also possible to have short memory but intrinsic type determination. Such cases would be hard to discriminate because twin experiments would show little correspondence in the types of twins, even though the state of the twins before the cue still largely determines the outcome.

It is unclear how a cell’s resistant type is determined. One view is that cells have fixed regulatory programs that lead to particular outcomes. Another view is that cells adapt to stress, leading to a wider range of outcomes, each of which may be determined by both the specific stress and the particular internal state of the cell at the time. Future work may reveal the molecular basis of this regulatory rewiring.

Here, we focused on characterizing resistant types of single-cell-derived cancer cells in the face of anti-cancer therapies. Our work joins a burgeoning literature on genetic and non-genetic sources of cellular heterogeneity in cancer. Cell line profiling has shown surprising levels of variability even in clonal lines, perhaps reflecting clonal memory[7,13,39–41]. Notably, this variability can drive a number of cancer phenotypes, including therapy resistance[1,10], growth[39], tumorigenicity[42], and metastasis[43]. FateMap could reveal a gamut of emergent types in several biological processes, including stem cell reprogramming and directed differentiation[33,44,45], and identify their potential origins.

Data Availability

All raw and processed imaging data generated in this study can be found on BioStudies (Accession S-BIAD696). All raw and processed FateMap single-cell barcoding data generated in this study can be found at Figshare (DOI 1: 10.6084/m9.figshare.22798952 ; DOI 2: 10.6084/m9.figshare.22802888). All raw and processed gDNA barcoding data generated in this study can be found at Figshare (DOI: 10.6084/m9.figshare.22806494). All raw and processed whole genome sequencing data of individual clones used in this manuscript can be found at BioProject Accession PRJNA972638 and figshare (10.6084/m9.figshare.23255273), respectively. All raw and processed bulk RNA Sequencing data used in this manuscript can be found at GEO Accession GSE233622. All raw and processed single-cell RNA Sequencing data used in this manuscript can be found at GEO Accession: GSE233766. All raw and processed data from the GeoMx spatial transcriptomics used in this manuscript can be found at BioProject Accession PRJNA976929 and Figshare (10.6084/m9.figshare.23248199), respectively.

Code Availability

All code used in this study is provided at the following DOI at Zenodo: https://doi.org/10.5281/zenodo.8000328

Acknowledgements

We thank Shweta Ramdas, Connie Jiang, Lauren Beck, Philip Burnham, Lee Richman, Madeline Melzer, Samuel Reffsin, Eduardo Torre, Chris Cote, Allison Cote, Vito Rebecca, and Grace Allard for insightful discussions related to this work. We thank the Genomics Facility at the Wistar Institute, especially Sonali Majumdar and Sandy Widura, for assistance with sequencing and single-cell partitioning and addition of 10X cell identifiers. We thank the Flow Cytometry Core Laboratory at the Children's Hospital of Philadelphia Research Institute for assistance with flow cytometry and fluorescence-activated cell sorting. We thank the Histology Core at the Penn Center for Musculoskeletal Disorders for their assistance with tissue sectioning (P30 AR069619). We thank the Center for Genetic Medicine, NUSeq Core, Feinberg Information Technology, Northwestern University Information Technology, and Quest High Performance Computing Cluster at Northwestern University Feinberg School of Medicine for their assistance. We thank Bhavana Singh for histotechnology expertise. We thank Indu Raman, Guangchun Chen, and Chengsong Zhu from the Microarray Core at UT Southwestern Medical Center in Dallas, TX for their expert help with Region Of Interest (ROI) selection on the GeoMx Digital Spatial Profiler (DSP) and data generation. We thank Jessie Villanueva, Rocio Inga, and Ling Li from the Herlyn Lab at the Wistar Institute for their assistance with identifying and obtaining the NRAS-mutant melanoma cell lines and the melanocyte cell line. YG thanks Robert J Valadka and Matt Temkin for their prompt support in setting up the wet and dry lab space at Northwestern University. MEF and ATW thank the Core Facilities of the Johns Hopkins Kimmel Cancer Center, P30CA00697356. YG acknowledges support from Northwestern University's startup funds, Research Catalyst Program from the McCormick School of Engineering at Northwestern University, Cancer Research Foundation Young Investigator Award, the Burroughs Wellcome Fund Career Awards at the Scientific Interface, the Jane Coffin Childs Memorial Fund, and the Schmidt Science Fellowship; GTB acknowledges support from NSF GRFP DGE-1845298; MP was supported by grants to YG including the Burroughs Wellcome Fund Career Awards at the Scientific Interface and Northwestern University's startup funds; RHB acknowledges support from NIH T32 HG000046 and T32 GM007170; EIG acknowledges support from the NSF NRT 2021900-Synthesizing Biology Across

Scales; BE acknowledges support from NIH F30 CA236129, NIH T32 GM007170, and NIH T32 HG000046; AK acknowledges support from NIH K00-CA-212437-02; NJ acknowledges support from NIH F30 HD103378; NB acknowledges support from NIH T32 GM144295; IAM acknowledges support from NIH F30 NS100595; KK acknowledges support from NIH T32 GM008216; PTR acknowledges support by NIH Medical Scientist Training Program T32 GM07170; DF and MH acknowledge support from NIH grants RO1 CA238237, U54 CA224070, PO1 CA114046, P50CA174523 and the Dr. Miriam and Sheldon G. Adelson Medical Research Foundation; SA was supported by grants to YG including the Burroughs Wellcome Fund Career Awards at the Scientific Interface, Northwestern University's startup funds, and Research Catalyst Grant from McCormick School of Engineering; CC was supported by grants to YG including the Burroughs Wellcome Fund Career Awards at the Scientific Interface and Northwestern University's startup funds; MEF and ATW acknowledge support from R01CA174746 and R01CA207935; ATW is also supported by a Team Science Award from the Melanoma Research Alliance and P01 CA114046; and AR acknowledges support from NIH Director's Transformative Research Award R01 GM137425, NIH R01 CA238237, NIH R01 CA232256, NIH P30 CA016520, NIH SPORE P50 CA174523, and NIH U01 CA227550.

Author Contributions

YG and AR conceived and designed the project. YG designed, performed, and analyzed all experiments, supervised by AR. MP, GTB, and EIG assisted YG with FateMap experiments and analysis. RHB, PTR, JL, and MP assisted YG with bulk RNAseq experiments and analysis. MP performed specific analysis for revisions with inputs from YG and AR. IPD, GTB, SSA, EIG, MCD, and CC assisted YG with tissue sectioning and automated RNA FISH and DAPI scans and analysis. YG, BE, and KK designed and optimized the PCR "side reaction" primers for recovering the barcodes from single-cell RNA sequencing libraries. RHB, GTB, and JL extracted genomic DNA for WGS experiments and NB performed the WGS analysis with inputs from YG and AR. AK assisted YG in the design and implementation of spheroid experiments. GTB, NJ, JL, JB, MP, and IAM assisted YG with barcode library preparation and computational pipeline. YG designed the mouse barcoding experiments, and DF, HL, YC, GMA, and MEF performed the mouse experiments with input from YG, MH, AR, and ATW. YG and GTB prepared barcode libraries for mouse experiments. MC, RHB, RGW, RL, DRI, SBJ, KW, MP, AJL, and JAW performed human patient experiments and analysis with inputs from YG and AR. YG, GTB, and EG prepared all illustrations used in this study. YG and AR wrote the manuscript with input from all authors.

Competing Interests

AR receives royalties related to Stellaris RNA FISH probes. YG received consultancy fees from the Schmidt Science Fellows and the Rhodes Trust. All other authors declare no competing interests.

Additional Information

For information regarding reprints, permissions, and requests for materials, please address correspondence to Yogesh Goyal (yogesh.goyal@northwestern.edu) and Arjun Raj (arjunrajlab@gmail.com).

References

1. Shaffer, S. M. *et al.* Rare cell variability and drug-induced reprogramming as a mode of cancer

drug resistance. *Nature* **546**, 431–435 (2017).

2. Rambow, F. *et al.* Toward Minimal Residual Disease-Directed Therapy in Melanoma. *Cell* **174**, 843–855.e19 (2018).
3. Schuh, L. *et al.* Gene Networks with Transcriptional Bursting Recapitulate Rare Transient Coordinated High Expression States in Cancer. *Cell Syst* **10**, 363–378.e12 (2020).
4. Roesch, A. *et al.* A temporarily distinct subpopulation of slow-cycling melanoma cells is required for continuous tumor growth. *Cell* **141**, 583–594 (2010).
5. Sharma, S. V. *et al.* A chromatin-mediated reversible drug-tolerant state in cancer cell subpopulations. *Cell* **141**, 69–80 (2010).
6. Gupta, P. B. *et al.* Stochastic state transitions give rise to phenotypic equilibrium in populations of cancer cells. *Cell* **146**, 633–644 (2011).
7. Shaffer, S. M. *et al.* Memory Sequencing Reveals Heritable Single-Cell Gene Expression Programs Associated with Distinct Cellular Behaviors. *Cell* **182**, 947–959.e17 (2020).
8. Emert, B. L. *et al.* Variability within rare cell states enables multiple paths toward drug resistance. *Nat. Biotechnol.* **39**, 865–876 (2021).
9. Su, Y. *et al.* Single-cell analysis resolves the cell state transition and signaling dynamics associated with melanoma drug-induced resistance. *Proc. Natl. Acad. Sci. U. S. A.* **114**, 13679–13684 (2017).
10. Spencer, S. L., Gaudet, S., Albeck, J. G., Burke, J. M. & Sorger, P. K. Non-genetic origins of cell-to-cell variability in TRAIL-induced apoptosis. *Nature* **459**, 428–432 (2009).
11. Elowitz, M. B., Levine, A. J., Siggia, E. D. & Swain, P. S. Stochastic gene expression in a single cell. *Science* **297**, 1183–1186 (2002).
12. Raj, A., Peskin, C. S., Tranchina, D., Vargas, D. Y. & Tyagi, S. Stochastic mRNA synthesis in mammalian cells. *PLoS Biol.* **4**, e309 (2006).
13. Kinker, G. S. *et al.* Pan-cancer single-cell RNA-seq identifies recurring programs of cellular heterogeneity. *Nat. Genet.* **52**, 1208–1218 (2020).
14. Rodriguez, J. *et al.* Intrinsic Dynamics of a Human Gene Reveal the Basis of Expression

Heterogeneity. *Cell* **176**, 213–226.e18 (2019).

15. Symmons, O. & Raj, A. What's Luck Got to Do with It: Single Cells, Multiple Fates, and Biological Nondeterminism. *Mol. Cell* **62**, 788–802 (2016).
16. Bhang, H.-E. C. *et al.* Studying clonal dynamics in response to cancer therapy using high-complexity barcoding. *Nat. Med.* **21**, 440–448 (2015).
17. Biddy, B. A. *et al.* Single-cell mapping of lineage and identity in direct reprogramming. *Nature* **564**, 219–224 (2018).
18. Weinreb, C., Rodriguez-Fraticelli, A., Camargo, F. & Klein, A. M. Lineage tracing on transcriptional landscapes links state to fate during differentiation. *bioRxiv* 467886 (2018) doi:10.1101/467886.
19. Gutierrez, C. *et al.* Multifunctional barcoding with ClonMapper enables high-resolution study of clonal dynamics during tumor evolution and treatment. *Nature Cancer* **2**, 758–772 (2021).
20. Oren, Y. *et al.* Cycling cancer persister cells arise from lineages with distinct programs. *Nature* **596**, 576–582 (2021).
21. Frieda, K. L. *et al.* Synthetic recording and in situ readout of lineage information in single cells. *Nature* **541**, 107–111 (2017).
22. Umkehrer, C. *et al.* Isolating live cell clones from barcoded populations using CRISPRa-inducible reporters. *Nat. Biotechnol.* **39**, 174–178 (2021).
23. Tian, L. *et al.* Clonal multi-omics reveals Bcor as a negative regulator of emergency dendritic cell development. *Immunity* **54**, 1338–1351.e9 (2021).
24. Leighton, J., Hu, M., Sei, E., Meric-Bernstam, F. & Navin, N. E. Reconstructing mutational lineages in breast cancer by multi-patient-targeted single cell DNA sequencing. *bioRxiv* 2021.11.16.468877 (2021) doi:10.1101/2021.11.16.468877.
25. Rodriguez-Fraticelli, A. E. *et al.* Single-cell lineage tracing unveils a role for TCF15 in haematopoiesis. *Nature* **583**, 585–589 (2020).
26. Pillai, M., Hojel, E., Jolly, M. K. & Goyal, Y. Unraveling non-genetic heterogeneity in cancer with dynamical models and computational tools. *Nature Computational Science* (2023).

27. Fennell, K. A. *et al.* Non-genetic determinants of malignant clonal fitness at single-cell resolution. *Nature* **601**, 125–131 (2022).
28. Marin-Bejar, O. *et al.* Evolutionary predictability of genetic versus nongenetic resistance to anticancer drugs in melanoma. *Cancer Cell* **39**, 1135–1149.e8 (2021).
29. Dardani, I. *et al.* ClampFISH 2.0 enables rapid, scalable amplified RNA detection in situ. *Nat. Methods* **19**, 1403–1410 (2022).
30. Ramirez, M. *et al.* Diverse drug-resistance mechanisms can emerge from drug-tolerant cancer persister cells. *Nat. Commun.* **7**, 10690 (2016).
31. Tirosh, I. *et al.* Dissecting the multicellular ecosystem of metastatic melanoma by single-cell RNA-seq. *Science* **352**, 189–196 (2016).
32. Krepler, C. *et al.* A Comprehensive Patient-Derived Xenograft Collection Representing the Heterogeneity of Melanoma. *Cell Rep.* **21**, 1953–1967 (2017).
33. Jiang, C. L. *et al.* Cell type determination for cardiac differentiation occurs soon after seeding of human-induced pluripotent stem cells. *Genome Biol.* **23**, 90 (2022).
34. Mold, J. E. *et al.* Clonally heritable gene expression imparts a layer of diversity within cell types. *bioRxiv* 2022.02.14.480352 (2022) doi:10.1101/2022.02.14.480352.
35. Torre, E. A. *et al.* Genetic screening for single-cell variability modulators driving therapy resistance. *Nat. Genet.* **53**, 76–85 (2021).
36. Das Thakur, M. *et al.* Modelling vemurafenib resistance in melanoma reveals a strategy to forestall drug resistance. *Nature* **494**, 251–255 (2013).
37. Algazi, A. P. *et al.* Continuous versus intermittent BRAF and MEK inhibition in patients with BRAF-mutated melanoma: a randomized phase 2 trial. *Nat. Med.* **26**, 1564–1568 (2020).
38. Richman, L. P., Goyal, Y., Jiang, C. L. & Raj, A. ClonoCluster: A method for using clonal origin to inform transcriptome clustering. *Cell Genomics* 100247 (2023).
39. Kuiken, H. J. *et al.* Clonal populations of a human TNBC model display significant functional heterogeneity and divergent growth dynamics in distinct contexts. *Oncogene* **41**, 112–124 (2022).
40. Ben-David, U. *et al.* Genetic and transcriptional evolution alters cancer cell line drug response.

Nature **560**, 325–330 (2018).

41. Meir, Z., Mukamel, Z., Chomsky, E., Lifshitz, A. & Tanay, A. Single-cell analysis of clonal maintenance of transcriptional and epigenetic states in cancer cells. *Nat. Genet.* **52**, 709–718 (2020).
42. Kröger, C. *et al.* Acquisition of a hybrid E/M state is essential for tumorigenicity of basal breast cancer cells. *Proc. Natl. Acad. Sci. U. S. A.* **116**, 7353–7362 (2019).
43. Naffar-Abu Amara, S. *et al.* Transient commensal clonal interactions can drive tumor metastasis. *Nat. Commun.* **11**, 5799 (2020).
44. Pour, M. *et al.* Epigenetic predisposition to reprogramming fates in somatic cells. *EMBO Rep.* **16**, 370–378 (2015).
45. Jain, N. *et al.* Retrospective identification of intrinsic factors that mark pluripotency potential in rare somatic cells. *bioRxiv* 2023.02.10.527870 (2023) doi:10.1101/2023.02.10.527870.

Main text captions

Fig. 1: FateMap reveals that between-clone fate type diversity arises from a single cell upon therapy treatment.

a. Schematic of single-cell-derived WM989 A6-G3 melanoma cells exposed to the targeted therapy drug vemurafenib, which formed resistant colonies in 3-4 weeks. Colonies were mixed together and single-cell sequenced.
b. Uniform Manifold Approximation and Projection (UMAP) algorithm applied to the first 50 principal components to visualize gene expression differences. 8,212 cells are colored by clusters determined using the FindClusters command: “Seurat clusters, resolution = 0.6”. n =1 of two biological replicates.
c. Cells on UMAP recolored by expression of a subset of differentially expressed genes. Genes with similar UMAP expression profiles are below each panel. *ACTA2* is found largely in Seurat cluster 8; *IFIT2* in 12; *VCAM1* in 15; *NGFR* in 7; *MLANA* in 0 and 3.
d. Schematic of FateMap for labeling cells with unique DNA barcodes before vemurafenib exposure. WM989 A6-G3 cells were transduced with FateMap barcode library at an MOI of ~0.15.
e. Barcoded cells were exposed to vemurafenib for 3-4 weeks and resultant colonies were single-cell RNA and barcode sequenced.
f. Are resistant cells sharing a barcode (a resistant clone) more transcriptionally similar to each other than other clones?
g. Clones, irrespective of their size, are constrained largely in specific clusters.
h. Quantification of preference for specific clusters across all clones (clone size>4; representative clones in yellow). Wilcoxon test (unpaired, two-sided), p-value < 2.2e-16.
i. RNA FISH of genes marking resistant types. Consistent with FateMap, we found resistant colonies selectively positive for each of the three markers tested, and negative for all.

Fig. 2: Gene expression differences between clones correspond to differences in morphology, proliferation, and invasiveness.

a. Classification of colonies as singletons, small colonies, or large colonies. Clusters exhibited different proliferative capacities.
b. Colony size distributions for each fate type. Mann Whitney/U test (unpaired, two-sided) was used, and the intervals are based on p-value thresholds = 0, 0.0001 (****), 0.001 (***), 0.01 (**), 0.05 (*). n =1 of two biological replicates.
c. (left) Schematics based on visual inspection of morphology, orientation, and density. (right) Brightfield images of resistant colonies exhibiting different morphologies.
d. Schematic of isolation and expansion of vemurafenib- or trametinib-resistant colonies, a subset of which were then bulk RNA sequenced, categorized for morphology, and measured for invasiveness.
e. Resistant cells were seeded at 3000 cells/well and allowed to form spheroids over 96-120 hours and were embedded in a collagen matrix. Red and cyan mark the invading and core boundary, respectively.
f. Invasiveness of resistant colonies emerging from treatment with trametinib quantified by computing the ratio of the area enclosing the red and cyan boundaries. Each dot represents one spheroid.

g. Mapping of morphology onto the FateMap data by comparing genes differentially expressed from morphology to resistant colonies. Similarity score on UMAP represents the degree of overlap of differentially expressed genes between bulk-sequencing data and each cluster. Resistant colony fate type 2 maps predominantly to cluster 7, while fate type 3 maps to cluster 15. Singletons, as identified by imaging for the *SOX10* gene, map to clusters 0 and 3.

Fig. 3: Resistant fate types emerge following targeted therapy in patients as evidenced by spatial transcriptomic profiling.

a. Overview of all 29 punch biopsies from four patients that were sequenced using the GeoMx Digital Spatial Profiler system for spatial transcriptomics. A total of 93 regions of interest were selected for sequencing based on visual inspection of DNA (SYTO 13, blue), CD45 (red), and S100B (green) staining. Two patient samples were coupled with matched pre-treatment biopsies (marked untreated).

b. Dot Plots of counts per million-(cpm)-transformed data for selected markers of resistant fate types as identified from in vitro FateMap. Each dot is a single region of interest colored by that region's qualitative S100B staining level, faceted by the punch biopsy of each region. Specific punch biopsies highlighting nearby regions with different expression profiles are highlighted for two patients, both pre- and post- treatment.

Fig. 4: Cells are predestined for distinct resistant fates upon exposure to therapy.

a. Schematic of FateMap "twin" experimental designs. We transduced WM989 A6-G3 cells (MOI ~0.15) with FateMap barcode library. After 3-4 cell divisions, we sorted the barcoded population, split the cells (A and B), treated each with vemurafenib, and performed single-cell RNA and barcode sequencing on the colonies (Supplementary Table 11).

b. Unique barcode abundance is identified by genomic DNA sequencing in splits A and B. Those present in both splits are dark blue (87), and those present in only (14 each) one are cyan. n =1 of two biological replicates.

c. (top) Venn diagram of overlap between barcode clones present in both splits (dark blue) compared to those present only in either A or B (cyan). (bottom) Comparison of the observed overlap between the shared barcodes (twins) surviving across splits with random survival chance (simulated 1,000 times).

d. UMAPs of representative twin clones (sharing the same barcode) across the two splits A (8,212 cells) and B (7,262 cells). The resistant twins largely end up with the same transcriptional fate type, invariant of the clone size.

e. Painting large clones onto the UMAP, where each color represents a unique resistant clone.

f. Mixing coefficient is used to calculate the pairwise transcriptional relatedness of clones (see Methods). Higher mixing coefficient corresponds to higher transcriptional relatedness of clones (1 = perfect mixing; 0 = no mixing). Representative UMAP examples are provided.

g. Mixing coefficient for twin clones across splits A and B is presented with representative examples on the UMAP.

h. Box-plots of comparison of cumulative mixing coefficients between clones within splits A (133) and B (102) (gray), non-twin clones across A and B (66) (gray), and twin clones (12) (blue). Wilcoxon test (unpaired, two-sided), p-value for non-twin compared to twin clones = 4.513e-08.

Fig. 5: Changing the therapy dose results in stereotypic resistant fate type switching and altered transcriptional profiles.

a. (left) Nuclei scans of resistant colonies emerging from treatment of 25,000 WM989 A6-G3 cells with two vemurafenib doses (1uM and 100nM). (right) Total colonies from each dose across n = 3 biological replicates.
b. Schematic of FateMap "twin" experimental designs for different vemurafenib doses. We transduced WM989 A6-G3 cells with the barcode library. After 3-4 cell divisions, we sorted the barcoded population, divided it into splits A and B, treated each with vemurafenib, and performed FateMap. We list three possible scenarios for outcomes (Cell counts available in Supplementary Table 11).
c. Combined low (13,400 cells) and high (9,457 cells) dose resistant cells obtained from UMAP applied to the first 50 principal components. Cells are colored by clusters determined using Seurat's FindClusters command.
d. UMAP with resistant cells colored by dose; dark and light blue represent high and low dose, respectively. Arrows represent regions present only in one dose.
e. UMAP is split by each dose, with colors representing clusters determined in c. Arrows represent clusters present only in the low or high dose.
f. UMAPs recolored for expression of genes *NGFR* and *MLANA*, markers for clusters enriched in one of the two doses.
g. (left) UMAP cluster colored for only cluster 9 (high for *NGFR*). (right) A pie chart to demonstrate that 25.3% of all the *NGFR*-high clones present in high dose were also detected in the low dose.
h. (left, middle) Representative examples of where twins from the *NGFR*-high cluster in the high dose go in the low dose. Fate type switch 1 (38/46) twins had similar fate types, as did fate type switch 2 (8/46) twins. (right) A cumulative density contour plot of fate type switches from high to low dose.

Methods

Cell lines and culture

WM989 A6-G3 and WM983b E9-C6 melanoma cell lines, first described in [8] and kindly provided by the lab of Dr. Meenhard Herlyn, were derived by twice single-cell bottlenecking the WM989 and WM983b melanoma cell lines respectively. The identities of WM989 A6-G3 and WM983B E9-C6 were verified[8] by DNA STR microsatellite fingerprinting at the Wistar Institute. WM989 A6-G3 5a3, first described in [35], was derived by single-cell bottlenecking of WM989 A6-G3. MDA-MB-231-D4, first described in [7] was derived by single-cell bottlenecking of MDA-MB-231 (ATCC HTB-26). The identity of MDA-MB-231-D4 was verified[7] by ATCC human STR profiling cell line authentication services. WM3451 P2G7 and WM3623 P4E7 were derived by single-cell bottlenecking WM3451 and WM3623 respectively, both of which were kindly provided by the lab of Dr. Meenhard Herlyn and verified by ATCC human STR profiling cell line authentication services.

FOM230-1 primary melanocytes were also kindly provided by the lab of Dr. Meenhard Herlyn. Briefly, they obtained foreskin tissue from the Cooperative Human Tissue Network. The foreskin was cut into pieces (approximately 5mm x 5mm), transferred into a tube containing dispase II, and incubated at 4°C for 15-18 hours. The next day the epidermis was separated from the dermis and the epidermal sheets were minced as small as possible. 0.05% trypsin was added, and the minced sheets were incubated at 37°C for 3-5 minutes depending on cell disaggregation. This mixture was then pipetted up and down vigorously to release single cells from the epidermal sheets. The trypsin was neutralized with soybean trypsin inhibitor and centrifuged for 5 minutes at 1,200 rpm at room temperature. The supernatant was aspirated to remove any remaining stratum corneum. The cell pellet was then resuspended with melanocyte growth medium.

WM989 A6-G3, WM989 A6-G3 5a3, WM983b E9-C6, WM3451 P2G7, and WM3623 P4E7 melanoma cell lines were cultured in TU2% media (80% MCDB 153, 10% Leibovitz's L-15, 2% FBS, 2.4mM CaCl2, 50 U/mL penicillin, and 50 µg/mL streptomycin). MDA-MB-231 cell lines were cultured in DMEM10% (DMEM with glutamax, 10% FBS and 50 U/mL penicillin, and 50 µg/mL streptomycin). All six cell lines were passaged using 0.05% trypsin-EDTA. FOM 230-1 melanocyte cells were cultured in Melanocyte Growth Medium (PromoCell, C-24010). Melanocytes were passaged using 0.05% trypsin-EDTA and neutralized using soybean trypsin inhibitor (Gibco, 17075-029).

Flow sorting of barcoded cells

We used 0.05% trypsin-EDTA (Gibco, 25300120) to detach the barcoded cells from the plate and subsequently neutralized the trypsin with the corresponding media depending on the cell type (Tu2% for WM989, WM983B, WM3451, and WM3623; DMEM + 10% FBS for MDA-MB-231; Melanocyte Growth Medium for FOM 230-1). We then pelleted the cells, performed a wash with 1X DPBS (Invitrogen, cat. 14190-136), and resuspended them again in 1X DPBS. Cells were sorted on a BD FACSJazz machine (BD Biosciences) or MoFlo Astrios (Beckman Coulter), gated for positive GFP signal and singlets. Sorted cells were then centrifuged to remove the supernatant media containing PBS, and replated with the appropriate cell culture media. Gating strategies are described in Supplementary Figure 17.

Drug treatment experiments

We prepared stock solutions in DMSO of 4 mM vemurafenib (PLX4032, Selleck Chemicals, S1267), 10 mM pinometostat (Selleck Chemicals, S7062), 100 μM trametinib (Selleck Chemicals, S2673), and 4mM paclitaxel (Life Technologies, P3456). We prepared small aliquots (10-15ul) for each drug and stored them at −20 °C to minimize freeze–thaw cycles. For drug treatment experiments, we diluted the stock solutions in culture medium to a final concentration of 1 μM and 100nM for vemurafenib; 4 μM for pinometostat; 5 nM, 10nM, and 25 nM for trametinib; and 1 nM for paclitaxel unless otherwise specified.

The dose of vemurafenib (1 μM) was chosen as per Shaffer et al. (Nature 2017), which was optimized for growth arrest without overt cytotoxicity. The doses of trametinib used were 5 nM for WM989 A6-G3, 10 nM for WM3623 P4E7, and 25nM for WM3451 P2G7. These doses were also chosen based on a dose curve to obtain virtually complete growth arrest.

WM989 A6-G3 and WM983b E9-C6 cells were treated with either vemurafenib or 5 nM trametinib for 3-4 weeks, and the media was replaced every 3-4d. Similarly, MDA-MB-231-D4 cells were treated with paclitaxel for 3-4 weeks, and the media was replaced every 3-4d. WM3623 P4E7 cells were treated with 10 nM trametinib for 3-4 weeks, and the media was replaced every 3-4d. WM3451 P2G7 cells were treated with 25 nM trametinib for 3-4 weeks, and the media was replaced every 3-4d. At the end of the treatment, surviving cells were trypsinized, neutralized, washed with 1X DPBS, and then either 1) pelleted and stored at -20ºC for gDNA extraction, or 2) resuspended in PBS for single-cell RNA sequencing experiments. In some cases, cells were also fixed for imaging at the end of the treatment. For pinometostat (DOT1L inhibitor) pre-treatment (before addition of vemurafenib), WM989 A6-G3 cells were treated for five days, replacing media once at day 3.

For continuous-discontinuous dosing experiments, WM989 A6-G3 cells were barcoded and plated as described above. Both arms of the experiment were treated with 1μM vemurafenib. The continuous dose arm was maintained in 1 μM vemurafenib for the entirety of the experiment, while the discontinuous arm was maintained in 1 μM vemurafenib for nine days before being switched to culture media without 1 μM vemurafenib. The discontinuous arm was then maintained in this drug-free culture media for 25 days before being switched back to culture media with 1 μM vemurafenib for the final five days of the experiment.

Quantifying homogeneity within a clone

To estimate the homogeneity in gene expression within a clone, we calculated the Spearman's correlation coefficient, based on the top 500 most variable genes, for each pair of samples present in a clone. A group of random cells having the same size as the clone were selected as a control. The average correlation coefficient was compared between each clone and its paired control, using a Wilcoxon signed rank test (two-sided, paired) .

Cell cycle and apoptosis analysis

To test the effect of cell cycle phase on clone size distribution in each cluster, we regressed out cell cycle genes. First, the cell cycle phase scores were estimated for each cell using the *CellCycleScoring* function in the Seurat package for the genes involved in G2/M phase and S phase[31]. The cell cycle scores were then regressed out from the gene expression using the *RegressOut* function in the Seurat package. This function models the expression levels of each gene based on the cell cycle score. The regressed out gene expression matrix is calculated as the residuals for this model (for each gene), and these values are used for downstream analysis such as dimensional reduction. We also calculated scores for apoptosis using *AUCell*[46]. *HALLMARK_APOPTOSIS,* and *KEGG_APOPTOSIS* genesets were obtained from the Molecular Signature DataBase (MSigDB, Broad Institute[47]).

Bulk RNA-seq (phenotypic drift)

To quantify the phenotypic drift between early and later stages of treatment, we calculated the pairwise Euclidean distance for each pair of early and late samples for a colony. The Euclidean distance was calculated for the top 500 most variable genes in the dataset. As a paired control for each resistant colony, an equal number of random early and late samples were selected, and the Euclidean distance between them was measured. The average Euclidean distance was compared for true pairs and random pairs to estimate the extent of phenotypic drift in the colony. The comparison was statistically tested using a Wilcoxon signed rank test.

Clonal genes and clone identification

Differentially expressed genes for each clone (with clone size > 1) were identified using *FindAllMarkers* function. Cut-off of log2(foldchange) >1 and Bonferroni-corrected p-value < 0.05 were used to identify clonal genes. For identification of clones, a support vector machine model was trained and tested on clones having more than 100 cells. Clones were sectioned into training and testing groups by randomly sampling 80% samples for the training group and classifying the rest as the testing group. The model was trained on expression levels of clonal genes. As a control, clone labels were shuffled for the training samples, and a support vector machine was trained on the randomized data.

Patient data analysis

Single cell RNA-sequenced patient samples from GSE72056[31] and patient-derived xenograft model of WM4007 cells derived from AJCC stage IV melanoma male 62-year-old patient (never treated with any drug or immune therapy prior to surgery/biopsy) treated with dabrafenib and trametinib (this study) were analyzed to test for differential expression of genes identified in cell lines using FateMap. Samples were clustered using *FindClusters* function at a resolution of 0.6 and differentially expressed genes were identified for the clusters using *FindAllMarkers* function. Cut-offs of log2(foldchange) > 1 and Bonferroni-corrected p-value < 0.05 were used to identify cluster genes. The extent of overlap in genes between each patient dataset and cell line dataset (FM01) was measured and statistically evaluated using a hypergeometric test (Fisher's Exact Test). The extent of overlap was also compared to the extent of overlap when an equal number of genes were randomly subsampled from a list of all sequenced genes. Subsampling was repeated 100 times.

Size distribution of clusters

A Chi-square test of Independence was used to test the null hypothesis that the marker-based clusters are *independent* of colony size. The test was run on a contingency matrix consisting of a number of singleton (colony size = 1), small (1< colony size < 4) and large (colony size ≥ 4) colonies for each marker-based cluster. Pearson residuals were estimated to quantify the deviation of colony size distribution from the null hypothesis.

Principal component analysis of drug resistant and naive WM989 A6-G3 melanoma cells

We used SCTransform to normalize and variance-stabilize the dataset and then performed principal component analysis using Seurat's RunPCA command. To get total variance for each dataset (i.e. both the naive cell dataset and the drug resistant cell dataset), we took the sum of the variance estimates per row of the SCT@scale.data matrix (where each row represented a gene). We calculated the eigenvalues by squaring the standard deviations per principal component stored by Seurat following PCA generation. To calculate the fraction of variance explained per principal component, we divided each of our eigenvalues by the total variance, using ggplot2 to plot the fraction of variance explained for each of the first 50 principal components. To estimate how much variance could be explained by pure chance, we also ran PCA on randomized data.

Cluster and Euclidean distance analysis of drug resistant and naive WM989 A6-G3 melanoma cells

To quantify whether the resistant population exhibited greater transcriptional heterogeneity as compared to the untreated populations, we measured the Euclidean distance[48–50] between clusters within each condition. We used single-cell RNA sequencing datasets from two untreated samples and two resistant samples. To control for cell numbers across datasets, we extracted the number of cells in each sample and calculated the minimum cell count of all four datasets. Since the number of cells doesn't vary much between the samples [min = 7262, max = 8420], we decided to randomly sample to the minimum of the number of cells, 7262, and perform 10 sampling rounds. After subsampling, we applied the Seurat function "SCTransform" to normalize and stabilize the variance of molecular count data, and calculated the principal components. Next, we calculated the neighborhood overlap (Jaccard index) between every cell based on the first 50 principal components using the Seurat function FindNeighbors. We then applied the seurat function FindClusters to identify cell clusters based on their shared nearest neighbor (snn). To demonstrate that our results do not depend on the chosen resolution, we clustered the cells from a resolution of 0.2 to 1 in 0.1 steps. For each resolution, we calculated the Euclidean distance between the identified clusters using the R library "scperturbR"[48]. The Euclidean distance compares the mean pairwise distance of cells across two different identified clusters to the mean pairwise distance of cells within each cluster. We used the first 50 principal components to calculate the Euclidean distance between cells. After getting the sample resolution combination number of clusters and Euclidean distance, we compared the number of clusters for a given resolution and the Euclidean distances for a given number of clusters.

Whole genome sequencing and processing of naive and drug resistant clones

Eight naive clones, one original clone, and sixteen resistant clones were sequenced at 30X depth with paired end Illumina sequencing. FASTQs were pre-processed and aligned to hg38 based on GATK4 best practices using an open-source WGS pipeline, Sarek v.3.0[51]. Variant calling was performed using the GATK HaplotypeCaller[52].

Variant annotation of naive and drug resistant clones

Variant files were merged and annotated using the OpenCravat tool[53]. With this tool, the functional consequences of variants were predicted using CADD v.1.6.1[54] where coding variants with scaled c-scores >15 were considered deleterious. This c-score cutoff is typical for analysis and is recommended by the authors for filtering (https://cadd.gs.washington.edu/info). Variants analyzed were all in protein-coding regions of the genome. Insertion and deletion variants for which CADD scores were unavailable were included in the analysis, except for those annotated as in-frame. Additionally, variants present in less than 20% of reads in a sample were removed from analysis in an effort to filter out variants that arose in clonal expansion.

To assess the potential for acquired genetic resistance to therapy, Fisher's exact test was performed on variants that were present in resistance clones, but not untreated clones ($p < 0.05$). Variants in genes implicated in resistance to Vemurafinib from COSMIC (https://cosmic-blog.sanger.ac.uk/drug-resistance-data-cosmic/) were independently analyzed for acquired genetic resistance. Variants in known epigenetic modifier genes[55] were also separately analyzed to evaluate heterogeneity. Finally, each clone's list of CADD > 15 variants were compared to all other clones for non-random overlap with the hypergeometric test ($p < 0.05$). All gene sets and associated details are provided in Supplementary Table 9.

Clinical cohort

Patient samples from this study were from the enrolled clinical trial (NCT02231775) were previously described[56]. In brief, patients aged ≥18 years with histologically proven clinical stage III or oligometastatic stage IV *BRAF* V600E/K melanoma deemed to be resectable by multidisciplinary consensus and measurable disease by RECIST 1.1 criteria were enrolled. Those randomized to the experimental arm which received 8 weeks of neoadjuvant dabrafenib (150 mg orally twice daily) plus trametinib (2 mg orally daily) before surgical resection, who failed to achieve a major pathologic response ($n = 4$). Pathologic responses were determined by histopathologic examination of the complete surgical specimen by a melanoma pathologist, including SOX10 immunostaining when necessary to confirm the presence or absence of viable melanoma cells. These patients were treated at The University of Texas MD Anderson Cancer Center and had tumor samples collected and analyzed under Institutional Review Board (IRB)-approved protocols. Notably, these studies were conducted in accordance with the Declaration of Helsinki and approved by The UT MD Anderson Cancer Center IRB.

Tumor microarray preparation and digital spatial profiling

Formalin fixed paraffin embedded (FFPE) tumor tissue blocks from four melanoma BRAF/MEK inhibitor treated melanoma patients from the above cohort treated were used to build a tissue microarray (TMA) block using the ATA-100 Advanced Tissue Arrayer (Chemicon International) at The University of Texas MD Anderson Cancer Center. Tissue samples included in the TMA were from pretreatment, on-treatment or surgical resection time points. The TMA block included a total of 36 cores each measuring 1 mm in diameter. Multi-sampling of the tissue block was performed to account for intra tumoral heterogeneity. TMA slides were then assayed using the Nanostring GeoMx digital spatial profiler (DSP) and probed with the human melanoma morphology kit (Syto13, S100B and CD45) and the human whole transcriptome atlas (WTA) on a fee for service basis by Nanostring Technologies (Seattle, WA) performed at the University of Texas Southwestern Medical Center. Three regions of interest (ROI) were selected per tumor core to capture inter- and intra-tumor heterogeneity.

NGS Library Preparation and Sequencing for GeoMx Spatial Transcriptomics

GeoMx NGS libraries were prepared per manufacturer's guidelines. In brief, after collection completed, aspirates in the collection plate were dried down at 65°C for 1 hour in thermal cycler with open lid and resuspended in 10 µL of nuclease-free water. 4 µL of rehydrated aspirates were mixed with 2 µL of 5×PCR Master Mix and 4µL of SeqCode primers, and PCR amplification was then performed with 18 cycles. The indexed libraries were pooled equally and purified twice with 1.2×AMPure XP beads (Beckman Coulter). The final libraries were evaluated and quantified using Agilent's High Sensitivity DNA Kit and Invitrogen's Qubit dsDNA HS assay, respectively. Total sequencing reads per DSP collection plate were calculated based on the NanoString DSP Worksheet. The libraries were subjected to 38 bp paired-end sequencing (PE38) on an Illumina NovaSeq 6000 system with a 100-cycle S1 kit (v1.5)

RNA Fluorescence In Situ Hybridization (FISH) on cells in plates

We performed single-molecule RNA FISH as previously described[57]. For the genes used in this study, we designed complementary oligonucleotide probe sets using custom probe design software (MATLAB) and ordered them with a primary amine group on the 3′ end from Biosearch Technologies (Supplementary Table 3 for probe sequences). We then pooled each gene's complementary oligos and coupled the set to Cy3 (GE Healthcare), Alexa Fluor 594 (Life Technologies) or Atto647N (ATTO-TEC) N-hydroxysuccinimide ester dyes.

The cells were fixed as follows: we aspirated media from the plates containing cells, washed the cells once with 1X DPBS, and then incubated the cells in the fixation buffer (3.7% formaldehyde in 1X DPBS) for 10 min at room temperature. We then aspirated the fixation buffer, washed samples twice with 1X DPBS, and added 70% ethanol before storing samples at 4ºC. For hybridization of RNA FISH probes, we rinsed samples with wash buffer (10% formamide in 2X SSC) before adding hybridization buffer (10% formamide and 10% dextran sulfate in 2X SSC) with standard concentrations of RNA FISH probes and incubating samples overnight with coverslips, in humidified containers at 37ºC. The next morning, we performed two 30-min washes at 37ºC with the wash buffer, after which we added 2X SSC with 50 ng/mL of DAPI. We mounted the sample(s) for imaging in 2X SSC.

Immunofluorescence and imaging

For NGFR staining of fixed cells, after fixation and permeabilization, we washed the cells for 10 min with 0.1% BSA/PBS, and then stained the cells for 30 min with 1:500 anti-NGFR APC-labeled clone ME20.4 (BioLegend, 345107). We washed the cells five times with 0.1% BSA/PBS and followed with one final wash with PBS for 2 min at room temperature. Fresh PBS was added prior to imaging. Wells were imaged either immediately or after storage in 4ºC overnight. All conditions (wells) were fixed, permeabilized, and stained at the same time with identical settings. Wells from the same plate were all imaged consecutively in the same imaging session.

For dpERK staining of fixed cells, after fixation and permeabilization, we used primary antibodies targeting dpERK (p44/p42 ERK D12.14.4E Cell Signaling, 4370). First, we rinsed cells twice for 5 min each time with 5% BSA in PBS (5% BSA-PBS) and then incubated in the dark at room temperature for 2 hours in 5% BSA-PBS 1:200 dpERK antibodies. Next, we washed the cells 5 X 5 min with 5% BSA-PBS and then incubated the cells at room temperature for 1 hour in 5% BSA-PBS containing 1:500 goat anti-rabbit secondary antibody conjugated to Alexa Fluor 594 (Cell Signaling, 8889). After the secondary incubation, we washed the cells 5 X 5 min with 5% BSA-PBS containing 50 ng/mL of DAPI and then replaced the wash buffer with fresh PBS and proceeded with imaging consecutively. All conditions (wells) were fixed, permeabilized, stained, and imaged at the same time with identical settings.

For colony counting via nuclei imaging, the cells were fixed by aspirating media from the plates containing cells, washing the cells once with 1X DPBS, and then incubating the cells in the fixation buffer (3.7% formaldehyde in 1X DPBS) for 10 min at room temperature. We aspirated the fixation buffer, washed samples twice with 1X DPBS, and added 70% ethanol before storing samples at 4ºC. Fixed cells were stained for nuclei by incubation in 2X SSC containing 50 ng/ml of DAPI and then imaged each well *via* a tiling scan at 10X magnification.

Barcode lentivirus library generation and diversity estimation

Barcode libraries were constructed as previously described[8], and the protocol is available at https://www.protocols.io/view/barcode-plasmid-library-cloning-4hggt3w. Briefly, we modified the LRG2.1T plasmid (gift from Dr. Junwei Shi) by removing the U6 promoter and single guide RNA scaffold. We then inserted a spacer sequence flanked by EcoRV restriction sites after the stop codon of GFP, subsequently digesting this vector backbone with EcoRV (NEB) and gel purifying the linearized vector. We ordered PAGE-purified ultramer oligonucleotides (IDT) containing 100 nucleotides with a repeating “WSN” pattern (W = A or T, S = G or C, N = any) surrounded by 30 nucleotides homologous to the vector insertion site (Supplementary Table 1). We subsequently used Gibson assembly followed by column purification to combine the linearized vector and barcode oligo insert. We performed nine electroporations of the column-purified plasmid into Endura electrocompetent *Escherichia coli* cells (Lucigen) using a Gene Pulser Xcell (Bio-Rad). We then allowed for their recovery before plating serial dilutions and seeding cultures for maxi-preparation. We incubated these cultures on a shaker at 225 rpm and 32ºC for 12-14 hours, pelleted the resulting cultures by centrifugation, and used the EndoFree Plasmid Maxi Kit (Qiagen) to isolate plasmid according to the manufacturer’s protocol. Barcode insertion was verified by polymerase chain reaction (PCR) on colonies from plated serial dilutions. We pooled the plasmids from the 9 separate cultures in equal amounts by weight before packaging into lentivirus.

To estimate the barcode library complexity, we performed three independent transductions (see below for details) on WM989 A6-G3 melanoma cell lines, extracted gDNA, sequenced the barcodes, and noted the total and overlapping barcodes between pairs of three independent transductions. We estimated the barcode library complexity with the equation used in mark and capture analysis: $k/K = n/N$, where k is number of recaptured barcodes that were marked, K is number of barcodes captured in the second pool, n is the number of barcodes marked in the first pool, N is the estimated barcode library complexity. Using this formula, we found the barcode diversity from three transductions to be 48.9, 54.4, and 63.3 million barcodes (Supplementary Figure 1; raw data and calculation scripts are within the link provided in Data and Code Availability).

Lentivirus packaging and transduction

We adapted previously described protocols to package lentivirus[8,35]. We first grew HEK293FT to near confluency (80-95%) in 10cm plates in DMEM containing 10% FBS and 50 U/mL penicillin, and 50 µg/mL streptomycin, and one day before plasmid transfection, we changed the media in HEK293FT cells to DMEM containing 10% FBS without antibiotics. For each 10cm plate, we added 80 µL of polyethylenimine (Polysciences, cat. 23966) to 500 µL of Opti-MEM (Thermo Fisher Scientific, cat. 31985062), separately combining 5 µg of VSVG and 7.5 µg of pPAX2 and 7.35 µg of the barcode plasmid library in 500 µL of Opti-MEM. We then incubated both solutions separately at room temperature for 5 min. We then mixed both solutions together by vortexing and incubated the combined plasmid-polyethylenimine solution at room temperature for 15 min. We added 1.09 mL of the combined plasmid-polyethylenimine solution dropwise to each 10cm dish. After 6-7 hours, we aspirated the media from the cells, washed the cells with 1X DPBS, and added fresh TU2% media. The next morning, we aspirated the media, and added fresh Tu2% media. Approximately 9-11 hours later, we transferred the virus-laden media to an empty, sterile 50ml tube and stored it at 4ºC, and added fresh Tu2% media to each plate. We continued to collect the virus-laden media every 9-11 hours for the next ~30 hours in the same 50ml tube, and stored the collected media at 4ºC. Upon final collection, we filtered the virus-laden media through a 0.45µm PES filter (MilliporeSigma SE1M003M00) and stored 1.5ml aliquots in cryovials at -80ºC.

To transduce WM989 A6-G3, WM983b E9-C6, WM3451 P2G7, WM3623 P4E7, FOM 230-1, and MDA-MB-231-D4 cells, we freshly thawed virus-laden media on ice, added it to dissociated cells, and plated ~100,000 cells/well in a six-well plate with ~3ml of the media. We then centrifuged the 6-well plate at 1,750 r.p.m. (517g) for 25 min. We then incubated the 6-well plate at 37ºC and replaced the media at ~8h, washed with 1X DPBS, and added fresh media (TU2% for WM989, WM983B, WM3451, and WM3623; Melanocyte Growth Media for FOM 230-1; and DMEM with 10% FBS for MDA-MB-231) to each well. After ~24 hours, we passaged the cells to 10-cm dishes, at which point we typically combined two wells by plating them together in a 10cm dish. For the FateMap experiments with WM989 A6-G3 melanoma cells exposed to vemurafenib, we planned to start each split with 600,000 barcoded/GFP-positive cells. The barcoded cells (GFP-positive) were then sorted and plated for a total of 4-5 population doubling until treatment with appropriate drugs. The time to 4-5 population doubling was 11-12 days for FOM 230-1, 10-11 days for WM989, WM3451, and WM3623 6-7 days for WM983B, 5-6 days for MDA-MB-231. The volume of the virus-laden media was decided by the titers performed on each cell line and target multiplicity of infection (MOI). For single-cell RNA sequencing experiments in particular, we targeted for the MOI to be ~10-25% to minimize the fraction of cells with multiple unique barcodes. We found it to be relatively computationally challenging to differentiate multiple-barcoded cells from doublets introduced by gel beads-in-emulsions.

Single-cell RNA sequencing

We used the 10X Genomics single-cell RNA-seq kit v3 to sequence barcoded cells. We resuspended the cells (targeting ~10,000 cells for recovery/ sample) in PBS and followed the protocol for the Chromium Next GEM Single Cell 3' Reagent Kits v3.1 as per manufacturer directions (10X Genomics, Pleasanton, CA). Briefly, we generated gel beads-in-emulsion (GEMs) using the 10X Chromium system, and subsequently extracted and amplified (11 cycles) barcoded cDNA as per post-GEM RT-cleanup instructions. We then used a fraction of this amplified cDNA (25%) and proceeded with fragmentation, end-repair, poly A-tailing, adapter ligation, and 10X sample indexing per the manufacturer's protocol. We quantified libraries using the High Sensitivity dsDNA kit (Thermo Fisher Q32854) on Qubit 2.0 Fluorometer (Thermo Fisher Q32866) and Bioanalyzer 2100 (Agilent G2939BA) analysis prior to sequencing on a NextSeq 500 machine (Illumina) using 28 cycles for read 1, 55 cycles for read 2, and 8 cycles for i7 index. A subset of FateMap sequencing runs (NRAS melanoma samples and Metronomic therapy experiments), we used NextSeq 2000 (Illumina) using 26 cycles for read 1, 124 cycles for read 2, and 8 cycles for i7 index.

Computational analyses of single-cell RNA sequencing expression data
We adapted the cellranger v3.0.2 by 10X Genomics into our custom pipeline (see Code Availability) to map and align the reads from NextSeq sequencing run(s). Briefly, we downloaded the bcl counts and used *cellranger mkfastq* to demultiplex raw base call files into library-specific FASTQ files. We aligned the FASTQ files to the hg19 human reference genome and extracted gene expression count matrices using *cellranger count*, while also filtering and correcting cell identifiers and unique molecular identifiers (UMI) with default settings.

We then performed the downstream single-cell expression analysis in Seurat v3. Within each experimental sample, we removed genes that were present in less than three cells, as well as cells with less than or equal to 200 genes. We also filtered for mitochondrial gene fraction which was dependent on the cell type. For non-identically treated samples, we integrated them using scanorama [58], which may work better to integrate non-similar datasets and avoid over-clustering. For samples that were exposed to identical treatment, we normalized using SCTransform [59] and the samples according to the Satija lab's integration workflow (https://satijalab.org/seurat/articles/integration_introduction.html). Using scanorama on identically-treated samples produced qualitatively similar results (Supplementary Figure 6).

For each experiment, we used these integrated datasets to generate data dimensionality reductions by principal component analysis (PCA) and Uniform Manifold Approximation and Projection (UMAP), using 50 principal components for UMAP generation. For a majority of analyses, we worked with the principal component space and normalized expression counts. For rare cases where we used Seurat UMAP clusters, we tested a range of resolutions with Seurat's FindClusters command. Our conclusions did not change qualitatively when we tested resolutions between 0.4 and 1.2 (Supplementary Figure 3). Details for all FateMap experiments, including total cell numbers and total barcoded cells per sample, are provided in Supplementary Table 11.

Bulk sequencing and analysis
We conducted standard bulk paired-end (37:8:8:38) RNA sequencing using RNeasy Micro (Qiagen 74004) for RNA extraction, NEBNext Poly(A) mRNA Magnetic Isolation Module (NEB E7490L), NEBNext Ultra II RNA Library Prep Kit for Illumina (NEB E7770L), NEBNext Multiplex Oligos for Illumina (Dual Index Primers Set 1) oligos (NEB E7600S), and an Illumina NextSeq 550 75 cycle high-output kit (Illumina 20024906), as previously described[1,60]. Prior to extraction and library preparation, the samples were randomized to avoid any experimental and human biases. As previously described, we aligned RNA-seq reads to the human genome (hg19) with STAR v2.5.2a and counted uniquely mapping reads with HTSeq v0.6.1[1,60,61] and outputs the count matrix. The counts matrix was used to obtain transcripts per million and other normalized values for each gene using custom scripts (see Code Availability).

To compare bulk sequencing data with single-cell RNA sequencing datasets, we first extracted differentially expressed genes for each single-cell RNA sequencing cluster (snn = 0.6) using the Seurat command FindAllMarkers, and filtering for adjusted p-value <0.05 and avg_logFC > 1. Similarly, we extracted differentially expressed genes for each condition of interest (morphology or invasiveness) and filtering for -1.5 < avg_logFC > 1.5. We then calculated the similarity score, which represents the normalized fraction of overlap of differentially expressed genes for the condition of interest between bulk-sequencing data and each single-cell RNA sequencing cluster.

Expanded resistant colonies morphology categorization

The resistant colonies were manually binned in one of the three categories based on the morphology images taken from the Nikon TS2-FL microscope: “small”, “on top”, and “not on top”. Those that were difficult to be binned in any category were labeled as “uncategorized”. Of the three categories, the “small” category was the most easy to identify manually and label due to characteristic optical and proliferation (slow growing) properties. The other two categories (“on top” and “not on top”) had further sets of morphological and proliferative differences, but were difficult to be parsed into specific categories. Of the 64 resistant colonies isolated and expanded across therapy treatments of vemurafenib and trametinib, five were uncategorized. The differentially upregulated genes for “small” and “on top” are provided in Supplementary Table 4. For category “not on top”, only four genes were differentially upregulated, thus precluding us from doing further analysis. Some resistant colonies did not survive the expansion process.

Nearest neighbor analysis

We developed a quantifiable approach to measure the gene expression relatedness of different barcoded clones. For each pair of barcoded clones, we calculated the nearest neighbors for each cell in the 50-dimensional principal component space. We then classified the neighbors as “self” if the neighbors are from the same barcode clone or “non-self” if they belong to the other barcode clone. We defined a quantifiable metric, the mixing coefficient, as follows:

$$mixing\ coefficient\ = \frac{number\ of\ non{-}self\ neighbors}{number\ of\ self\ neighbors}$$

A mixing coefficient of 1 would indicate perfect mixing such that each cell has the same number of self and non-self neighbors. A mixing coefficient of 0 would indicate that there is no mixing and that each cell within a barcoded clone lies far away from the other barcoded clone in the principal component space. The higher the mixing coefficient, the higher the transcriptional relatedness of the barcoded clones analyzed. As the number of nearest neighbors depends on the size (number of cells) of a clone, we performed this analysis between cells of similar clone size (Supplementary Figure 14). Within a specified size range, we normalized the number of neighbors per barcode clone to account for small size differences. The number of neighbors to extract was chosen to be a minimum of 10 or the size of the smaller of the two barcode clones.

Barcode recovery from single-cell RNA sequencing data

As the barcodes are transcribed, we extracted the barcode information from the amplified cDNA from 10X Genomics V3 chemistry protocol (step 2). We ran a PCR side reaction with one primer that targets the 3’ UTR of GFP and the other that targets a region introduced by the amplification step within the V3 chemistry of 10X genomics (“Read 1”). The two primers amplify both the 10X cell-identifying sequence as well as the 100 bp barcode that we introduced lentivirally. The number of cycles, typically between 12-15, are decided by the Ct value from a qPCR reaction (New England Biolabs M0543) for the specified cDNA concentration. The thermal cycler (Veriti 4375305) was set to the following settings: 98 °C for 30 s, followed by N cycles of 98 °C for 10 s and then 65 °C for 2 min and, finally, 65 °C for 5 min. Upon completion of the PCR reaction, we immediately performed a 0.7X bead purification (Beckman Coulter B23318) followed by final elution in nuclease-free water. Purified libraries were quantified with High Sensitivity dsDNA kit (Thermo Fisher) on Qubit Fluorometer (Thermo Fisher), pooled, and sequenced on a NextSeq 500. We sequence 26 cycles on Read 1 which gives 10X cell-identifying sequence and UMI, 124 cycles for read 2 which gives the barcode sequence, and 8 cycles for index i7 to demultiplex pooled samples. The primers used are provided in Supplementary Table 2.

Experiments in mice

For each experiment, WM989 cells were uniquely barcoded with protocols as described above and allowed to divide 4-5 times before splitting the barcoded pool into five groups, each containing an equal number of cells. We aimed for ~1-1.5 million WM989 cells to be injected per mice. All animal experiments were performed in accordance with institutional and national guidelines and regulations. The protocols have been approved by the Wistar IACUC. WM989 cells in serum-free RPMI 1640 media (Corning 10-40-CM) were mixed in a 1:1 ratio with Growth Factor Reduced Matrigel® (Corning 354230), then were subcutaneously implanted into the flanks of NSG mice. Once tumors reached about $100mm^3$ per caliper measurement, animals were randomized into treatment groups. Treatment consisted of Low Dose 41.7 mg PLX4720/kg diet (Research Diets D21051202i), or High Dose 417 mg PLX4720/kg diet (Research Diets D21051201i), to which they had constant access. PLX4720 is closely related both structurally and biologically to PLX4032, which was used for *in vitro* experiments, and also targets the same molecule and BRAF-V600E structural configuration. As PLX4720 continues to be the drug used in mouse xenograft models and has a similar half-life to PLX4032 (Kaur et al., Nature, 2016; and Torre et al., Nature Genetics 2021), we used PLX4730 instead of PLX4032 for *in vivo* experiments. Tumor size was measured by calipers every 2-4 days, and tumor volumes were calculated according to the equation 0.5*L*W*W, where L is the longest side and W is a line perpendicular to L. Mice were sacrificed once tumors reached 1500 mm^3, and once one mouse reached the endpoint, all mice from the same barcode pool were sacrificed regardless of tumor size. The tumor tissue was snap frozen in liquid N_2 for genomic DNA extraction. We had 5 biological replicate experiments. We could not extract sufficient gDNA from experiments 3 and 4, and these were excluded from barcode split population analysis.

Computational analyses of barcoded single-cell datasets

The barcodes from the side reaction of single-cell cDNA libraries were recovered by developing custom shell, R, and python scripts (see Code Availability). Briefly, we scan through each read searching for sequences complementary to the side reaction library preparation primers, filtering out reads that lack the GFP barcode sequence, have too many repeated nucleotides, or do not meet a phred score cutoff. Since small differences in otherwise identical barcodes can be introduced due to sequencing and/or PCR errors, we merged highly similar barcode sequences using STARCODE software[62], available at https://github.com/gui11aume/starcode. For varying lengths of barcodes (30, 40 or 50, see the pipeline guide provided) depending on the initial distribution of Levenshtein distance of non-merged barcodes, we merged sequences with Levenshtein distance ≤ 8, summed the counts, and kept only the most abundant barcode sequence. The decision to use a Levenshtein distance ≤ 8 was reached by systematically analyzing the difference between experimentally observed mean Levenshtein distance with the theoretically provided mean Levenshtein distance for a pair of barcodes. We then compared various Levenshtein distances and found that a Levenshtein distance ≤ 8 resulted in the least difference between observed and expected mean distances between barcodes. Results from this analysis are provided in Supplementary Figure 2.

For next processing steps and downstream analysis, we first filtered out all barcodes that were associated below the minimum cutoff (dependent on sequencing depth) of unique molecular identifiers (UMI). We next removed all barcodes where one 10X cell-identifying sequence was associated with more than one unique barcode. This could either result from multiplets introduced within gel beads-in-emulsions or because of the same cell receiving multiple barcodes during lentiviral transduction. After these two filtering steps, we were able to recover barcodes associated with 50-60% of single cells, which were then used to do the downstream clone-resolved analysis.

Barcode library preparation and sequencing from genomic DNA

We prepared barcode libraries from genomic DNA (gDNA) as previously described[8]. Briefly, we isolated gDNA from barcoded cells using the QIAmp DNA Mini Kit (Qiagen, cat. 51304) per the manufacturer's protocol. Extracted gDNA was stored as a pellet in -20ºC for days to weeks before the next step. We then performed targeted amplification of the barcode using custom primers containing Illumina adaptor sequences, unique sample indices, variable-length staggered bases, and an 'UMI' consisting of 6 random nucleotides (NHNNNN). As reported in [8], the 'UMI' does not uniquely tag barcode DNA molecules, but nevertheless appeared to increase reproducibility and normalize raw read counts. We determined the number of amplification cycles (N) by initially performing a separate quantitative PCR (qPCR) and selecting the number of cycles needed to achieve one-third of the maximum fluorescence intensity for serial dilutions of genomic DNA. The thermal cycler (Veriti 4375786) was set to the following settings: 98°C for 30 s, followed by N cycles of 98°C for 10 s and then 65°C for 40 s and, finally, 65 °C for 5 min. Upon completion of the PCR reaction, we immediately performed a 0.7X bead purification (Beckman Coulter B23318), followed by final elution in nuclease-free water. Purified libraries were quantified with a High Sensitivity dsDNA kit (Thermo Fisher) on a Qubit Fluorometer (Thermo Fisher), pooled, and sequenced on a NextSeq 500 using 150 cycles for read 1 and eight cycles for each index (i5 and i7). The primers used are provided in Supplementary Table 6.

Analyses of sequenced barcodes from genomic DNA

The barcode libraries from genomic DNA sequencing data were analyzed as previously described[8], with the custom barcode analysis pipeline (see Code Availability). Briefly, this pipeline searches for barcode sequences that satisfy a minimum phred score and a minimum length. Note that we count the total number of 'UMIs' as described in the gDNA library chemistry above. These 'UMIs' do not necessarily tag unique barcode DNA molecules, but empirically they slightly improve correlation in barcode abundance among replicate libraries[8]. We also use STARCODE[62], available at https://github.com/gui11aume/starcode, to merge sequences with Levenshtein distance ≤ 8 and add the counts across collapsed (merged) barcode sequences.

In this current work, we also created two subclones (D8 and F8) of WM989 A6-G3, with each clone carrying a unique barcode sequence (Supplementary Table 7). We used these two clones as standards to convert sequencing counts into actual cell numbers which significantly reduces the PCR and cell number bias across samples. We spiked in a known number of cells from each of the two barcoded clones to each cell pellet before gDNA extraction and sequencing. We then used linear regression (on (0,0), (count_F8, cells_F8), (count_D8, cells_D8)) to get the conversion factor from read counts of all barcodes to their actual cell numbers. We used a minimum cell count and log2-fold change between pairs of conditions to annotate clones as condition-dependent or condition-independent. We found that changing the cutoff for minimum cell count did not affect our conclusions (Supplementary Figure 15).

Simulation for barcode overlap

We adapted a described previously computational model that simulates all steps of our experiments designed to compare barcode overlap in resistant colonie [63]. The model simulates cell seeding and infection. Each cell is represented as an independent object. The number of barcoded cells was calculated as

$$number\ of\ barcoded\ cells\ =\ number\ of\ seeded\ cells\ \times\ (1-e^{-MOI})$$

where the MOI was estimated for our barcode lentivirus. Barcodes were represented by integer numbers from among 50 million variants of unique barcodes estimated from our lentiviral library diversity (see Methods and Supplementary Figure 1). The subset of barcoded cells was assigned barcodes randomly with replacement from this library. The model simulates expanding cells prior to addition of the drug. Each cell, regardless of barcode status, undergoes a cell division procedure with 4-5 rounds depending on the experimental condition. In each round, a given cell will give rise to a number of progeny sharing the same barcode based on an estimated distribution of cell division. The model plates cells onto separate dishes/splits (total dishes/splits dependent on the experiment) by randomly assigning each cell an integer. The model simulates the formation of resistant colonies assuming a purely stochastic model of resistance. A defined fraction of cells on each plate form resistant colonies based on an resistance efficiency that was calculated as

$$resistance\ efficiency\ =\frac{number\ of\ barcoded\ resistant\ colonies\ after\ drug\ course}{number\ of\ seeded\ barcoded\ cells}$$

based on experimental observations. Additionally, each cell forming a resistant colony is subject to a probabilistic material loss at different stages of the *in silico* experiment, including cell culture (5% both *in vivo* and *in vitro*), genomic DNA extraction (0% *in vitro* and 10% *in vivo* mouse), DNA sequencing library preparation (5% both *in vivo* and *in vitro*), and (as needed) mouse injection (15%) and tumor extraction (15%). The output of the model was the number of barcodes shared between different plates or barcode overlap. This was not corrected for cells having more than one lentiviral barcode due to multiple integrations for a given MOI. We performed 1000 and 200 independent simulations for *in vitro* and *in vivo* experiments respectively to obtain a distribution of barcode overlap values to determine the probability of obtaining our observed barcode overlap from our experiments by random chance. This model was written and executed in R.

Tissue sectioning and RNA FISH

We adapted the protocol described previously[64]. Tumor tissue extracted from mice subcutaneously injected with WM989 A6-G3 5a3[35] was mounted in Tissue-Plus O.C.T. compound (Fisher Healthcare), flash-frozen in liquid nitrogen, wrapped in aluminum foil, and then stored tissues at −80°C. Tissues were cryosectioned at 6 or 8 μm using a Leica CM1950 cryostat within the Center for Musculoskeletal Disorders (PCMD) Histology Core. We adhered tissue samples to positively charged Superfrost Plus slides (Fisher Scientific). We then washed slides in PBS, fixed them in 4% formaldehyde for 10 min at room temperature, then washed them two times in PBS. Fixed slides were stored in 70% ethanol in LockMailer microscope slide jars at 4°C.

For RNA FISH on tissue sections, we placed the slide in the wash buffer (2X SSC, 10% formamide) and allowed it to equilibrate for 2-3 min. We then removed slides from the wash buffer and dried off the slides with kimwipes. Immediately after drying, we added 500-1000 µL of 8% SDS to the tissue section on the slide for 1 min. After 1 min, we turned the slide on the side to remove the SDS, transferred the slide to the wash buffer, and kept it in the wash buffer for ~2 min. We then tapped down the wash buffer on a kimwipe or paper towel, added 50 µL of probe-containing hybridization buffer (10% dextran sulfate, 2X SSC, 10% formamide) as a drop in center of tissue sample, and placed a cover slip on top of the tissue section. We then placed the slide into a humidifying chamber to prevent the slide from drying, and placed the chamber containing slides in a 37ºC incubator overnight. We took out the chamber to RT the next day and placed the slide with coverslip into a wash buffer container and let the cover slip come off. We then transferred the slides to a container or LockMailer jar containing wash buffer and incubated for 30 min at 37ºC. We removed it from the 37ºC incubator and performed a second incubation with wash buffer and DAPI, and put it back into 37ºC for another 30 min. We performed one final wash in wash buffer, rinsed two times in 2X SSC, and added 50-100 µL of 2X SSC to the tissue section. We then placed a coverslip on the tissue, sealed it with nail varnish, and let it dry before imaging. We used clampFISH data on tissue sections (Supplementary Figures 12 and 13) from another study, and detailed methods on clampFISH protocols are provided in [29].

Spheroid assay

We adapted the protocol described previously[65]. Tissue culture–treated 96-well plates were coated with 50 µL 1.5% Difco Agar Noble (Becton Dickinson). Melanoma cells were seeded at 3000 cells/well and allowed to form spheroids over 96 to 120 hours. Spheroids were harvested and embedded using collagen type I (GIBCO, #A1048301). The collagen plug was prepared as 300 µL mix per layer, and two layers were added into each well [1X Eagle Minimum Essential Medium (EMEM; 12-684, Lonza); 10% FCS; 1X l-glutamine; 1.0 mg/mL collagen I; NaHCO3 (17-613E, Lonza), diluted in PBS as required]. The first layer was added to each well and allowed to solidify. After 5 to 10 min, spheroids were mixed with the remaining 300 µL mix and added to the well to solidify. Once the plug was solidified, media were added to the well and incubated at 37°C at 5% CO2 and imaged after 24 hours and 48 hours. Spheroid images were acquired on a Nikon Ti2E inverted microscope. Quantitation of invasive surface area was performed using NIS Elements Advanced Research software. Of the 64 resistant colonies we expanded, only 24 colonies had enough cells to form multiple spheroids per colony. Of these 24, 6 did not form spheroids and 2 only had one spheroid each. Of the remaining 16 colonies, 8 colonies belonged to resistant colonies emerging from trametinib, 3 belonged to 1µM vemurafenib and 5 belonged to 250nM vemurafenib. The differentially upregulated genes for “fast invading” and “slow invading” are provided in Supplementary Table 5.

Imaging

To image RNA FISH and nuclei signal, we used a Nikon TI-E inverted fluorescence microscope equipped with a SOLA SE U-nIR light engine (Lumencor), a Hamamatsu ORCA-Flash 4.0 V3 sCMOS camera, and 4X Plan-Fluor DL 4XF (Nikon MRH20041/MRH20045), 10X Plan-Fluor 10X/0.30 (Nikon MRH10101) and 60X Plan-Apo λ (MRD01605) objectives. We used the following filter sets to acquire different fluorescence channels: 31000v2 (Chroma) for DAPI, 41028 (Chroma) for Atto 488, SP102v1 (Chroma) for Cy3, 17 SP104v2 (Chroma) for Atto 647N, and a custom filter set for Alexa 594. We tuned the exposure times depending on the dyes used (Cy3, Atto 647N, Alexa 594, and DAPI). For large tiled scans, we used a Nikon Perfect Focus system to maintain focus across the imaging area. For imaging RNA FISH signals in tissue sections, we acquired z-stacks (three positions) at 60X magnification, and used maximum intensity projection to visualize the signal. For brightfield imaging of resistant colonies, we used a Nikon Eclipse Ts2-FL with an Imagingsource DFK 33UX252 camera and 4X Plan-Fluor 4X/0.13 (Nikon MRH20041) objective. For time-lapse imaging of the emergence of drug-resistant colonies, we used an IncuCyte S3 Live Cell Imaging Analysis System (Sartorius) with a 4X objective on WM989 A6-G3 tagged with an mCherry nuclear reporter (H2B-mCherry).

Image processing

For colony counting, all image processing was done blind to the condition (either drug type/dose or with/without DOT1L inhibition). The wells (within the 6-well plates) were pseudo-named in a format independent from drug or dose. Nikon-generated nd2 files were first parsed using custom MATLAB scripts (rajlabformattools) to convert them from nd2 format to tiff format (see Code Availability). Images for each well were then stitched using custom MATLAB code and the number of cells in each well was counted using custom MATLAB code with a Gaussian filter consistent across samples being compared (colonycounting_v2). Colonies within each well were manually segmented and MATLAB was used to calculate the total number of colonies, cells per colony, and cells outside of colonies (see Code Availability). The summary average counts for each colony is provided in Supplementary Table 10. RNA FISH and clampFISH on tissue sections were quantified using a custom built computational pipeline, also used in other previous studies [1,29]. The code is provided with the Zenodo DOI.

For immunofluorescence, all image processing was done blind to drug conditions; the wells were pseudo-named in a format independent from drug or dose. Nikon images were first stitched using Nikon Elements software. The channels were split in Fiji and scaled to a smaller size compared to their original pixel size prior to placing them in illustrator. For the conditions being compared (e.g. each well with a different drug dose/type), the individual channels were equally adjusted for brightness and contrast across each pair of wells for the signal of interest. Raw nd2 files are provided for each imaging experiment which contains additional metadata for image settings. For the images taken on the brightfield microscope Nikon TS2FL, the scale bar lengths were calculated by using the pixel size given by the manufacturer of the camera. For well images taken on the Nikon TI-E inverted fluorescence microscope, the scale bar lengths were calculated using Nikon Elements software to add a line of a specific length to the images.

Estimation of survival fraction in MDA-MB-231-D4

We estimated the frequency of drug resistance in MDA-MB-231-D4 by computing the fraction of surviving barcoded colonies upon treatment with paclitaxel as compared to the total number of uniquely barcoded cells in the initial population. From two separate split population experiments, we obtained the frequency to be 1:956 and 1:1303 (see Data and Code Availability for the script).

Vemurafenib resistant colony isolation and expansion

WM989 A6-G3 cells were treated with 1μM vemurafenib (PLX4032, Selleck Chemicals, S1267) for four weeks to allow resistant colonies to form and expand. Plates with resistant colonies were scanned under a tissue culture microscope to identify colonies that were physically distant from other colonies or singletons. The distant colonies were imaged with a 4X objective, physically isolated, and dissociated via treatment with 0.05% trypsin for 5-10 minutes as some colonies took longer to detach than others. Colony suspensions were plated in 12-well plates containing 1mL of TU2% media containing 1µM vemurafenib, and the media was changed the following day to remove residual trypsin. Isolated resistant colonies were closely monitored for growth daily, and the 1µM vemurafenib containing media was changed every 3-5 days. Isolated resistant colonies were expanded into 10cm and then 15cm plates when cells reached 70-80% confluence. When expanding from 12-well plates to 10cm plates, 75,000 cells were harvested for RNAseq. When cells reached 70-80% confluence in 15cm plates, 75,000 cells were harvested for a later time point of RNAseq.

Silencing Plate Cell Culture, Imaging, & Analysis

Drug-naive WM989 A6-G3s were transduced with unique barcodes as described above. Cells were plated in 6 well plates at a density of 100,000 cells/well. One plate was formaldehyde fixed after 24 hours using a protocol described above and the second plate was treated with media containing 1µM PLX after 24 hours. This drug treatment was continued for three weeks which was enough time for resistant colonies to form. This second plate containing resistant populations was formaldehyde fixed. Wells were imaged on a Nikon TI-E inverted fluorescence microscope equipped with a SOLA SE U-nIR light engine (Lumencor), a Hamamatsu ORCA-Flash 4.0 V3 sCMOS camera, and 10X Plan-Fluor 10X/0.30 (Nikon MRH10101). Images were analyzed using the custom Raj Lab image processing software NimbusImage via the CellPose tool[66]. Average intensity for each of the cells was calculated also using NimbusImage.

Whole Genome Sequencing Cell Culture, Isolation, and Expansion

WM989 A6-G3 cells that were frozen as a backup from the original experiments were thawed and passaged three times before bottlenecking. Cells were trypsinized, centrifuged and resuspended to a concentration of either .5 cells/200 µL, 1 cell/200 µL, or 2 cells/200 µL. One full 96 well plate was used for each dilution. Plates were imaged on an Incucyte S3 24 hours after the cells were plated. The plates were scanned again 2 days after the first scan and 7 days after the second scan. Any wells that did not definitively have a single cell in the first scan were excluded from the experiment. Once clones had reached ~90% confluency in the 96 well plate, they were scaled up to a 24 well plate. This process was repeated to 12 well, 6 well, and 10cm plates. Ultimately, 8 unique clones were generated for whole genome sequencing.

NRAS Cell Line Drug Treatment & Imaging

WM3451 P2G7 and WM3623 P4E7 cell lines were imaged during drug treatment to track morphological changes and colony formation. Cells were plated in 10 cm dishes at a density of 300,000 cells/dish. Media was changed 15 hours after plating for media containing 10 nM trametinib (WM3623 P4E7) or 25 nM trametinib (WM3451 P2G7). Media was changed and brightfield images were taken of the cells every 3-4 days, and this was continued for 5 weeks.

Patient Sample GeoMx Analysis

Segments for spatial sequencing were drawn based on manual inspection of S100B and CD45 staining using the NanoString GeoMx Digital Spatial Profiler software and sequenced as per the GeoMx protocol. Sequencing data was processed and subjected to quality control using the manufacturer's proprietary software. Quality control analysis was performed using the manufacturer's suggested default values except where otherwise noted. Briefly, segments with fewer than 1000 reads, less than 80% aligned reads and less than 50% sequencing saturation were excluded from further analysis. Biological probes were excluded from the target count calculation if the ratio of the geometric mean of the probe in all segments to the geometric mean of the probe in the target was less than or equal to 0.1 or if the probe failed the Grubbs outlier test in 20% or more of samples. Finally, we kept targets that exceeded a threshold (higher of limit of quantification or count of two) in at least 5% of samples. The filtered target counts were exported to R and counts were normalized using the Trimmed Means of M values method. Count per million values for selected genes based on *in vitro* resistant fate types were then plotted for each segment.

GeoMx variable gene overlap with FateMap resistant fate type markers

The unsupervised cell clusters in the FM01 dataset were annotated with the resistant cell fate types shown in Figure 1. The data was subset to include only cells that had a resistant fate type label, and the Seurat command *FindAllMarkers* with the options ‘only.pos =TRUE’ was run on the resulting subset dataset. The filter p_val_adj < 0.05 was applied to the resulting marker list, and the top 100 marker genes for each of the five resistant fate types were chosen as the top 500 markers. The coefficient of variation (CV) for each gene across patient and sample type (pre-treatment or resistant) was calculated for each gene in the GeoMx data. The GeoMx data was then subset to include only genes expressed in the WM989 cells used in the FM01 experiment. Boxplots were generated in R comparing the CVs of the top 500 FateMap markers to all other genes. P values were computed using the two-sided, unpaired Wilcoxon test.

Resistant fate type GeoMx uneven partitioning analysis

The unsupervised cell clusters in the FM01 dataset were annotated with the resistant cell fate types shown in Figure 1 and the object was subset to include only those cells. The Seurat command *AverageExpression* with options “return.seurat = F, assays = 'SCT', slot = 'counts'” was used to generate a gene signature matrix for each resistant fate type for downstream deconvolution. The SCT-normalized counts were transformed into log-transformed counts per million values via the Trimmed Means of M method to match the GeoMx data. The following process was then repeated once per patient. Two ROIs on the same plug were chosen. We calculated a weighted mean of their transcriptomes using the number of nuclei from the GeoMx metadata. The gene signature matrix and the original and average ROI transcriptomes were then subset to only include genes common to all datasets and in common with FM01 differentially expressed genes. This was done to improve deconvolution by removing noisy, uninformative genes. The original and average ROI transcriptomes were deconvoluted using non-negative least squares deconvolution to yield resistant fate type cell proportions. These proportions were multiplied by the number of nuclei to give an estimated number of cells in each ROI and the ‘combined’ ROI with the mean transcriptome. An observed Euclidean distance between the two original ROIs is then calculated by reversing the deconvolution on each of the two original ROIs.

From the estimated cell numbers, two analyses are performed. The first analysis generates a null distribution of euclidean distances in which cells from the combined ROI are binomially distributed to two ROIs and the deconvolution is reversed to re-generate transcriptomes and calculate the euclidean distance between them. This sampling is done 10,000 times, and the null distribution is compared to the observed distance and the probability of a sampling a distance greater than the observed is calculated. Second, the estimated cell numbers in the combined ROI are partitioned in groups of 10 into either ROI 1 or ROI 2 in all possible combinations that add up to the true number of cells in each ROI +/- 2%. For each partition, the deconvolution is reversed and the euclidean distance is calculated between the transcriptomes. For each partition, we also calculate the mean absolute deviation away from 50-50 (equal partitioning) for all cell fate types. We compare whether the calculated euclidean distance is at least as large as the observed distance between the original ROIs, and find the mean absolute deviation away from 50-50 for the 25th percentile of distances at least as large as the observed distance.

RNA FISH of Resistant Colonies Derived from WM989 A6-G3 and Two Clonal Lines

WM989 A6-G3 and two subclones thereof, WM989 A6-G3 A10 and WM989 A6-G3 A11, were used to generate vemurafenib-resistant colonies. Cells were plated in glass-bottom 6 well plates and media was changed 18 hours after plating for media with 1μM vemurafenib (PLX4032, Selleck Chemicals, S1267). Media was changed every 3-4 days. WM989 A6-G3 A10 and WM989 A6-G3 A11 plates were fixed after 4 weeks of drug treatment and the WM989 A6-G3 plate was fixed after 5 weeks of drug treatment. Cells were fixed, hybridized with FISH probes, and imaged as described above.

Estimation of number of cell divisions

Cell culture was initiated at 25% confluency and cells were allowed to divide until they reached 75 to 80% confluency. The WM989 A6-G3 cells were passaged a total of 10 times, and each passage followed similar confluency at initial (right after nth passage) and final (right before n+1th passage) time points. To estimate the number of divisions, we assume all cells at a given time point can divide to form two daughter cells.

$$0.25N * 2^{n} = 0.75N$$

$$N * 2^{n} = 3N$$

$$n = log_{2}3$$

$$n = 1.58$$

Where, N is the number of cells at 100% confluency and n is the number of division cells undergo when cultured from 25% confluency upto 75% confluency. Therefore, cells divide approximately 1 to 2 times during a passage. For 10 passages, we can estimate the dynamics to be equivalent to the population expanding 3-fold ten times:

$$N * 2^{n'} = 3^{10}N$$

$$2^{n'} = 3^{10}$$

$$n' = log_{2}3^{10}$$

$$n' = 15.85$$

where n' is the number of division cells undergo when cultured from 25% confluency up to 75% confluency through 10 passages. Therefore, the cells underwent approximately 16 divisions over the 10 passages for WM989 A6-G3 between initial clonal isolation and our analysis. A similar calculation for the A10 and A11 subclones, which underwent 12 passages, yielded an estimate of 19 divisions.

Phenotypic Volume and Shannon's Equitability Index

To estimate the transcriptional variability of cells within a clone or within a cluster, phenotypic volume (PV) was estimated as described in Fennell et al., 2021. The log of PV was quantified as the sum of all non-zero eigenvalues for the singular value decomposition of the covariance matrix for gene expression. The covariance matrix was calculated for the scaled gene expression matrix for differentially expressed genes identified by FateMap. As a randomized control, barcodes or cluster numbers for cells were shuffled and the phenotypic volume was re-calculated. Normalized phenotypic volume was estimated as the difference between the phenotypic volume for a clone or a cluster and its paired random control divided by the phenotypic volume for the paired random control.

To quantify the distribution of each clone across the UMAP clusters, Shannon's Equitability Index was quantified for each clone and a paired random control (created by shuffling barcodes). Shannon's Equitability Index was calculated as:

$H = -\Sigma p\mathrm{i} * \ln(p\mathrm{i}) / \ln(\mathrm{S})$

where, H is Shannon's Equitability Index, p_i is the probability of finding cells in the i^{th} cluster and S is the number of clusters. Shannon's Equitability Index ranges from 0 to 1. A value of 1 indicates that the cells in a clone are evenly spread across all clusters. A value of 0 indicates that all cells in a clone are present in a single cluster.

References

46. Aibar, S. *et al.* SCENIC: single-cell regulatory network inference and clustering. *Nat. Methods* **14**, 1083–1086 (2017).
47. Subramanian, A. *et al.* Gene set enrichment analysis: a knowledge-based approach for interpreting genome-wide expression profiles. *Proc. Natl. Acad. Sci. U. S. A.* **102**, 15545–15550 (2005).
48. Peidli, S. *et al.* scPerturb: Information Resource for Harmonized Single-Cell Perturbation Data. *bioRxiv* 2022.08.20.504663 (2022) doi:10.1101/2022.08.20.504663.
49. Replogle, J. M. *et al.* Mapping information-rich genotype-phenotype landscapes with genome-scale Perturb-seq. *Cell* **185**, 2559–2575.e28 (2022).
50. Székely, G. J. & Rizzo, M. L. Energy statistics: A class of statistics based on distances. *J. Stat. Plan. Inference* **143**, 1249–1272 (2013).
51. Garcia, M. *et al.* Sarek: A portable workflow for whole-genome sequencing analysis of germline and somatic variants. *F1000Res.* **9**, 63 (2020).
52. Poplin, R. *et al.* Scaling accurate genetic variant discovery to tens of thousands of samples. *bioRxiv* 201178 (2018) doi:10.1101/201178.
53. Pagel, K. A. *et al.* Integrated Informatics Analysis of Cancer-Related Variants. *JCO Clin Cancer Inform* **4**, 310–317 (2020).

54. Rentzsch, P., Witten, D., Cooper, G. M., Shendure, J. & Kircher, M. CADD: predicting the deleteriousness of variants throughout the human genome. *Nucleic Acids Res.* **47**, D886–D894 (2019).

55. Singh Nanda, J., Kumar, R. & Raghava, G. P. S. dbEM: A database of epigenetic modifiers curated from cancerous and normal genomes. *Sci. Rep.* **6**, 19340 (2016).

56. Amaria, R. N. *et al.* Neoadjuvant plus adjuvant dabrafenib and trametinib versus standard of care in patients with high-risk, surgically resectable melanoma: a single-centre, open-label, randomised, phase 2 trial. *Lancet Oncol.* **19**, 181–193 (2018).

57. Raj, A., van den Bogaard, P., Rifkin, S. A., van Oudenaarden, A. & Tyagi, S. Imaging individual mRNA molecules using multiple singly labeled probes. *Nat. Methods* **5**, 877–879 (2008).

58. Hie, B., Bryson, B. & Berger, B. Efficient integration of heterogeneous single-cell transcriptomes using Scanorama. *Nat. Biotechnol.* **37**, 685–691 (2019).

59. Hafemeister, C. & Satija, R. Normalization and variance stabilization of single-cell RNA-seq data using regularized negative binomial regression. *Genome Biol.* **20**, 296 (2019).

60. Mellis, I. A. *et al.* Responsiveness to perturbations is a hallmark of transcription factors that maintain cell identity in vitro. *Cell Syst* **12**, 885–899.e8 (2021).

61. Dobin, A. *et al.* STAR: ultrafast universal RNA-seq aligner. *Bioinformatics* **29**, 15–21 (2013).

62. Zorita, E., Cuscó, P. & Filion, G. J. Starcode: sequence clustering based on all-pairs search. *Bioinformatics* **31**, 1913–1919 (2015).

63. Yunusova, A. M., Fishman, V. S., Vasiliev, G. V. & Battulin, N. R. Deterministic versus stochastic model of reprogramming: new evidence from cellular barcoding technique. *Open Biol.* **7**, (2017).

64. Symmons, O. *et al.* Allele-specific RNA imaging shows that allelic imbalances can arise in tissues through transcriptional bursting. *PLoS Genet.* **15**, e1007874 (2019).

65. Kaur, A. *et al.* Remodeling of the Collagen Matrix in Aging Skin Promotes Melanoma Metastasis and Affects Immune Cell Motility. *Cancer Discov.* **9**, 64–81 (2019).

66. Stringer, C., Wang, T., Michaelos, M. & Pachitariu, M. Cellpose: a generalist algorithm for cellular segmentation. *Nat. Methods* **18**, 100–106 (2021).

Extended Data Figure captions

Extended Data Figure 1: FateMap reveals that between-clone fate type diversity, albeit to a lesser degree, in treatment-naive cells.

a. (left) UMAP of all barcoded treatment-naive cells. Total 16,432 cells (8,420 split A and 8,012 cells in split B) are colored by clusters determined using Seurat's FindClusters command at a resolution of 0.6 (i.e. "Seurat clusters, resolution = 0.6"). (right) On the UMAP, we recolored each cell by its expression for a select subset of genes that were identified as differentially expressed in drug resistant cells *via* the Seurat pipeline (Cell counts available in Supplementary Table 11).
b. Five representative examples demonstrate that a clone (cells sharing the same barcode) is constrained largely in a specific transcriptional cluster such that cells within a clone are more transcriptionally similar to each other than cells in other clones.
c. Average pairwise correlation between cells within a clone was estimated based on the expression levels of the top 500 most variable genes. Each point represents the average value for Spearman's correlation coefficient for all possible pairs of cells within a clone. For each clone, a paired control was created by randomly sampling an equivalent number of cells from the entire population. Higher average correlation coefficient in clones indicates higher transcriptional similarity among cells within a clone, as compared to cells that are not clones. Wilcoxon signed rank exact test (paired, two-sided) was used to compare the difference in average correlation coefficient.
d. Fraction of variance explained by the experimental data and randomized data for the top 50 principal components (PCs). The number of PCs needed to explain the actual variance in data (indicated by the dotted line) is a measure of the degrees of freedom of variability of a given dataset. There was an increase (see Extended Data Figure 1E for statistical testing) in the number of PCs needed to explain the variance in data from resistant cells (43 PCs) as compared to naive (30 PCs) and primed cells (23 PCs), suggesting that there is an increase in overall variability in samples when cells transition to becoming drug resistant. Primed cells were identified as cells where at least 40% of pre-resistant markers identified in (Emert et al. 2021) are higher than their average expression level.
e. Average number of PCs needed to explain the variance in resistant, naive and pre-resistant cells. Error bars represent standard deviation over 100 simulations of randomized data. Mann-Whitney U-Test was used to estimate a p-value for pairwise difference in means.
f. Comparison of Euclidean distances between clusters across resistant and naive populations of melanoma cells for varying numbers of clusters. We used the first 50 principal components to calculate the Euclidean distance between cells across clusters. We used Wilcoxon signed rank exact test (paired, two-sided) for statistical comparisons.
g. Comparison between resistant and naive populations for total number of clusters, given fixed number of cells and shared nearest neighbor (snn) resolution. We used Wilcoxon signed rank exact test (paired, two-sided) for statistical comparisons of average number of clusters across resolutions.
h. UMAPs of representative twin clones (sharing the same barcode) across the two splits A and B. The twins largely end up with the same transcriptional fate. This observation suggests that cells have similar transcriptional states prior to drug treatment.

Extended Data Figure 2: Whole genome sequencing of treatment-naive and drug resistant fate type clones.

a. We performed a pairwise hypergeometric test for variants in all clones to determine statistical significance of variant overlap between clones. This was calculated with the following parameters (M = all CADD > 15 variants, n = # Variants in Sample 1, N = # Variants in Sample 2, X = # Variants in intersection of Samples 1 & 2). P-values are plotted on the heatmap where the p-value represents the probability of observing at least as large an overlap as observed if the two clones in fact had independently randomly selected variants from the full list of CADD > 15 variants. P-values below 0.05 represent two clones that are not genetically independent.
b. Heatmap of genes with deleterious variants (CADD > 15) that were present with allele frequencies between 25% and 75% in both naive and resistant clones, colored by their CADD deleteriousness score. For genes that include multiple, unique variants, the variants were collapsed into one row, where the variant with the highest CADD score was plotted for that sample. The curated gene set represents the lack of variation in (Shaffer et al. 2017; Garman et al. 2017). Differentially expressed genes from the FateMap dataset show eight genes with variation.
c. The expression patterns of the eight genes from the DEG list from FateMap with heterogeneously present genetic variants, visualized on UMAP (Cell counts available in Supplementary Table 11).
d. To evaluate for acquired genetic resistance to therapy in the resistant clones, we next plotted variants on a heatmap (colored by their CADD deleteriousness score) if there was a significant difference in the allele frequencies of variants between naive and resistant clones by Fisher's exact test ($P < 0.05$). Variants were only included if they were not present in any naive clones. The curated gene set represents the lack of acquired variants in genes from [2017 paper genes], [FateMap DEG], [Clone Genes], [Top 500 most Variable Genes], [Known Epigenetic Modifiers]. The ["all variants with CAAD>15"] includes all variants with CADD c-scores over 15.
e. We analyzed 143 genes classified as epigenetic modifiers for deleterious variants (CADD>15) within naive clones. The chart shows the number of genes with variants in a subset of naive clones (2 genes) and in all naive clones (10 genes).
f. Heatmap of deleterious variants in epigenetic modifier genes, colored by their CADD deleteriousness score.

Extended Data Figure 3: Isolation, longitudinal profiling and functional mapping of drug resistant clones.

a. Schematic for longitudinal tracking and profiling of drug resistant colonies. Colonies were isolated, expanded and maintained over 4 to 6 weeks. Paired initial and late samples were sequenced at a bulk-level.
b. Paired initial and late samples display minimal phenotypic drift in principal component (PC) space for top 500 most variable genes. Insets show brightfield images of representative samples.
c. Euclidean distance (in PC1 and PC2) measured between paired initial and late samples and equivalent number of random initial-late pairs of samples. Lower Euclidean distance in true pairs as compared to random pairs implies that paired initial and late samples are transcriptionally more similar (closer in PC space) than any pair of initial and late samples.
d. Scree plot depicting cumulative variance explained by PCs. Dotted line represents that most of the variance can be explained by the first 25 PCs alone.

e. Euclidean distance (in first 25 PCs) measured between paired initial and late samples and equivalent number of random initial-late pairs of samples. Lower Euclidean distance in true pairs as compared to random pairs implies that paired initial and late samples are transcriptionally more similar (closer in PC space) than any pair of initial and late samples.
f. Euclidean distance measured between paired early and late samples and equivalent number of random initial-late pairs of samples. Euclidean distance was measured in PC1 and PC2 space for top 200, 500 and 1000 variable genes.
g. Euclidean distance measured between paired initial and late samples and equivalent number of random initial-late pairs of samples. Euclidean distance was measured in the PC space created by the first 25 PCs for top 200, 500 and 1000 variable genes.
h. Mapping of invasiveness onto the single-cell RNA sequencing dataset from FateMap by comparing genes differentially expressed between the two slowest and the two fastest invading resistant colonies (UMAP colored for similarity score). The slowest invading colonies have a high similarity score for cluster 15 (and to some extent 4 and 6), while the fastest invading colonies have a high similarity score for cluster 8 (and to some extent 1).

Extended Data Figure 4: FateMap on BRAF and NRAS mutant melanoma cell lines reveals between-clone fate type diversity.

a. (left) For another single-cell derived melanoma cell line WM983B E9-C6, we traced representative resistant cells in Adobe Illustrator and created cartoon schematics based on visual inspection of orientation and density. (right) Brightfield images of resistant colonies exhibiting different types of morphologies.
b. We applied the Uniform Manifold Approximation and Projection (UMAP) algorithm within Seurat to the first 50 principal components to visualize differences in gene expression. Cells are colored by clusters determined using Seurat's FindClusters command at a resolution of 0.5 (i.e. "Seurat clusters, resolution = 0.5") (13,869 and 11,249 total cells respectively for split A and B).
c. On the UMAP, we recolored each cell by its expression for a select subset of genes that were identified as differentially expressed via the Seurat pipeline and marked different clusters. *MLANA*, which marks melanocytes, is found largely in clusters 1,3, and 5; *IFIT2*, which marks type-1 interferon signaling, is found largely in cluster 4; *NGFR*, which marks neural crest cells, is found largely in cluster 2 and 4; *AXL*, which is a canonical resistance marker, is found largely in cluster 5 and 7.
d. Six examples to demonstrate that a clone (cells sharing the same barcode) is constrained largely in a specific transcriptional cluster such that cells within a clone are more transcriptionally similar to each other than cells in other clones. Some clones are larger in size than others, and some exist as singletons, meaning they survive vemurafenib treatment but do not necessarily divide while exposed to the drug.
e. We quantified the preference for a specific cluster across all barcode clones (clone size>4). Specifically, we calculated the fraction of dominant clusters for each clone and found it to be significantly higher (Wilcoxon test, two-sided, unpaired, p-value = 1.49e-15) than that for randomly selected cells. The analysis plotted here is for a cluster resolution of 0.5.
f. Painting of singletons and colonies onto the UMAP demonstrated that singletons and colonies belonged to distinct regions and clusters.
g. UMAPs of representative twin clones (sharing the same barcode) across the two splits A and B. The twins largely end up with the same transcriptional fate type, invariant of the clone size.

This observation suggests that cells are predestined for distinct resistant fate types upon exposure to vemurafenib.

h. NRAS mutant cell line WM3623 treated with three different doses of trametinib (10 nM, 20 nM, and 40 nM). Representative brightfield images after 2.5 and 5 weeks of drug treatment are shown for each dose.
i. (left) UMAP of all barcoded 3623 cell line cells treated with Trametinib. 6,397 cells are colored by clusters determined using Seurat's FindClusters command at a resolution of 0.6 (i.e. "Seurat clusters, resolution = 0.6"). (right) On the UMAP, we recolored each cell by its expression for a select subset of genes that were identified as differentially expressed in drug resistant cells via the Seurat pipeline.
j. On the UMAP, we recolored each cell by its expression for a select subset of genes that were identified as differentially expressed in drug resistant cells via the Seurat pipeline.
k. Five representative examples demonstrate that a clone (cells sharing the same barcode) is constrained largely in a specific transcriptional cluster such that cells within a clone are more transcriptionally similar to each other than cells in other clones.
l. UMAPs of representative twin clones (sharing the same barcode) across the two splits A (6,397 cells) and B (7,538 cells). The twins largely end up with the same transcriptional fate type. This observation suggests that drug resistant cells are derived from the same clones having similar transcriptional states and are constrained in the gene expression space. One of the clones appears to be a dominant clone and gives rise to a large fraction of sequenced cells.

Extended Data Figure 5: FateMap on an NRAS mutant melanoma cell line reveals between-clone fate type diversity.

a. NRAS mutant cell line WM3451 treated with three different doses of trametinib (20 nM, 40 nM, and 50 nM). Representative brightfield images after 2.5 and 5 weeks of drug treatment are shown for each dose.
b. (left) UMAP of all barcoded 3451 cells treated with Trametinib. 5,789 cells are colored by clusters determined using Seurat's FindClusters command at a resolution of 0.6 (i.e. "Seurat clusters, resolution = 0.6"). (right) On the UMAP, we recolored each cell by its expression for a select subset of genes that were identified as differentially expressed in drug resistant cells via the Seurat pipeline.
c. Five representative examples demonstrate that a clone (cells sharing the same barcode) is constrained largely in a specific transcriptional cluster such that cells within a clone are more transcriptionally similar to each other than cells in other clones.
d. Average pairwise correlation between cells within a clone was estimated based on the expression levels of the top 500 most variable genes. Each point represents the average value for Spearman's correlation coefficient for all possible pairs of cells within a clone. For each clone, a paired control was created by randomly sampling an equivalent number of cells from the whole population. Higher average correlation coefficient in clones indicates higher transcriptional similarity among cells within a clone, as compared to cells that are not clones. Wilcoxon signed rank test (paired, two-sided) was used to compare the difference in average correlation coefficient.
e. UMAP of all barcoded WM3451 P2G7 cells treated with Trametinib. Cells are colored by whether they are a singleton (i.e. clone size = 1).

f. UMAPs of representative twin clones (sharing the same barcode) across the two splits A (5,789 cells) and B (7,473 cells). The twins largely end up with the same transcriptional fate type. This observation suggests that drug resistant cells are derived from the same clones having similar transcriptional states and are constrained in the gene expression space.

Extended Data Figure 6: FateMap on treatment-naive primary human melanocytes reveals between-clone diversity.

a. (left) UMAP of all barcoded naive primary melanocyte cells. Cells are colored by clusters determined using Seurat's FindClusters command ("Seurat clusters, resolution = 0.6"). (right) On the UMAP, we recolored each cell by its expression for a select subset of genes that were identified as differentially expressed in drug resistant cells via the Seurat pipeline.
b. Six representative examples demonstrate that a clone is constrained largely in a specific transcriptional cluster such that cells within a clone are more transcriptionally similar to each other than cells in other clones.
c. Average pairwise correlation between cells within a clone was estimated based on the expression levels of the top 500 most variable genes. Each point represents the average value for Spearman's correlation coefficient for all possible pairs of cells within a clone. For each clone, a paired control was created by randomly sampling an equivalent number of cells from the whole population. Higher average correlation coefficient in clones indicates higher transcriptional similarity among cells within a clone, as compared to cells that are not clones. Wilcoxon signed rank test (paired, two-sided) was used to compare the difference in average correlation coefficient.
d. UMAP of all barcoded naive primary melanocyte cells. 2,868 cells are colored by whether they are a singleton (i.e. clone size = 1). Cluster 10 is enriched for singletons and displays high expression of S100B, a marker identified to be associated with single cell colonies by FateMap.
e. UMAPs of representative twin clones (sharing the same barcode) across the two splits A (2,868 cells) and B (3,333 cells). The twins largely end up with the same transcriptional fate type. This observation suggests that primary melanocyte cells derived from the same clone have similar transcriptional states and are constrained in the gene expression space.

Extended Data Figure 7: FateMap on a triple negative breast cancer cell line reveals between-clone fate type diversity.

a. Nuclei scans (DAPI-stained) of resistant colonies emerging from treatment of the single-cell derived triple negative breast cancer cell line MDA-MB-231-D4 with 1nM paclitaxel.
b. For the MDA-MB-231-D4 cell line, we traced representative resistant cells in Adobe Illustrator and created cartoon schematics based on visual inspection of orientation and density.
c. Brightfield images of resistant colonies exhibiting different types of morphologies.
d. We applied the Uniform Manifold Approximation and Projection (UMAP) algorithm within Seurat to the first 50 principal components to visualize differences in gene expression. 6,535 cells are colored by clusters determined using Seurat's FindClusters command ("Seurat clusters, resolution = 0.5").
e. We observed silencing of the transcribed barcodes in a subset of colonies, as revealed by epifluorescence imaging of the GFP signal. The colony on the left is strongly expressing a GFP signal while the colony on the right has a very dim GFP signal.

f. Cells with assigned barcodes were evenly distributed throughout the UMAP with no clear bias for any specific resistant fate types.
g. Four examples from split A (6,535 cells) demonstrate that a clone is constrained largely in specific UMAP regions such that cells within a clone are more transcriptionally similar to each other than cells in other clones.
h. Four examples from split B (8,745 cells) demonstrate that a clone is constrained largely in specific UMAP regions such that cells within a clone are more transcriptionally similar to each other than cells in other clones.
i. We quantified the preference for a specific cluster across all barcode clones (clone size>4). Specifically, we calculated the fraction of dominant clusters for each clone and found it to be significantly higher (Wilcoxon, unpaired, two-sided) than that for randomly selected cells. The analysis plotted here is for a cluster resolution of 0.5.
j. We found that our UMAP had superclusters defined by cell cycle (S, G1, G2M). Of the 3,720 clonal DEGs, 63 are cell cycle genes. We therefore regressed out cell cycle genes and the cell-cycle-genes-regressed data with UMAP.
k. We quantified the preference for a specific cluster across all barcode clones after cell cycle regression (clone size>4). Specifically, we calculated the fraction of dominant clusters for each clone and found it to be significantly higher (Wilcoxon, unpaired, two-sided) than that for randomly selected cells. The analysis plotted here is for a cluster resolution of 0.5.
l. UMAPs of representative twin clones across the two splits A and B. The twins largely end up with the same transcriptional fate type, invariant of the clone size. This observation suggests that cells are predestined for distinct resistant fate types upon exposure to chemotherapy drug paclitaxel.

Extended Data Figure 8: FateMap reveals differences in clonal fate type outcomes between continuous and discontinuous therapy.

a. Schematic of the experimental design where we exposed single-cell-derived WM989 A6-G3 melanoma cells to continuous and discontinuous doses of targeted therapy drug vemurafenib.
b. UMAP of all barcoded cells. 17,634 cells are colored by clusters determined using Seurat's FindClusters command ("Seurat clusters, resolution = 0.6").
c. Pellet morphology for continuous (7,238 cells) and discontinuous (10,396 cells) treatment cells. Cells derived from discontinuous dosage have a larger and darker (more pigmented) pellet. This suggests that during discontinuous dosage, melanocytic cells (which are pigmented in nature) proliferate.
d. On the UMAP, we recolored each cell by its expression for a select subset of genes that were identified as differentially expressed in drug resistant cells via the Seurat pipeline.
e. UMAP of all barcoded cells. Cells are colored by type of dosage.
f. UMAPs of representative twin clones (sharing the same barcode) that arise during discontinuous drug treatment. The twins largely end up with the same transcriptional fate type and have varying proliferative capacities.
g. In discontinuous dosage, 68% of clones having high *MLANA* expression (log2 Expression > 2, in at least 50% of cells in a given clone) are proliferative (i.e. have clone size > 1). In continuous dosage, only 20% of clones having high *MLANA* expression are proliferative.
h. (left) Total number of cells analyzed consisted of 60.5% discontinuous dosage samples and 39.5% continuous dosage samples. (right) The number of unique barcodes (i.e. resistant

clones) displays a 3.6 fold increase in discontinuous dosage sample as compared to the continuous dosage sample.

i. UMAPs of representative twin clones across the two splits of continuous and discontinuous dosing. Some twins end up in the similar transcriptional fate type while others tend to switch fate type.

Extended Data Figure 9: Changing the therapy type to trametinib eliminates an additional resistant fate type present in the vemurafenib treatment.

a. UMAP where the resistant cells are colored by the associated therapy drug type, with dark blue representing vemurafenib (9,457 cells) and light blue representing trametinib (8,569 cells). Arrows represent UMAP regions that are present only in vemurafenib or trametinib.
b. UMAP is split by each drug type, with colors representing clusters determined using Seurat's FindClusters command("Seurat clusters, resolution = 0.5"). Arrows represent UMAP regions that are present only in vemurafenib or trametinib.
c. Painting of singletons and colonies onto the UMAP, colored by the condition, demonstrated that singletons largely belong to vemurafenib and are present predominantly in the *MLANA*-high cluster. Colonies are dispersed more across the UMAP with no particular region enriched for either condition except for the *NGFR*-high cluster.
d. Imaging of nuclei (DAPI-stained) of resistant colonies emerging from treatment of WM989 A6-G3 cells to either vemurafenib or trametinib. The number of singletons in trametinib treated cells appear to be much less than those treated with vemurafenib, consistent with the sequencing data from FateMap.
e. Quantification of the total number of colonies and singletons from each drug type of imaging data across biological replicates. This analysis demonstrated that while the total number of colonies are similar across the two drug types, there is a relative increase (~2.45-fold; n = 3 biological replicates) in the number of singletons in the case of vemurafenib.
f. UMAPs are recolored for each cell by its expression for gene *MLANA*, which is a marker for cluster 3 relatively enriched in vemurafenib (as shown with arrows in A and B).
g. A pie chart to demonstrate that of all the clones (barcodes) present in vemurafenib-treated split in cluster 3, only 4.8% were also present in the trametinib-treated split.
h. A cumulative density contour plot capturing the types of fate switches that the *MLANA*-high cluster 3 clones from the vemurafenib-treated split adopt in the trametinib-treated split.
i. Three representative examples of UMAP regions where twins from the *MLANA*-high cluster 3 in the vemurafenib-treated split adopt in the trametinib-treated split.
j. UMAPs are recolored for each cell by its expression for gene *NGFR*, which is a marker for cluster 4 relatively enriched in trametinib (as shown with arrows in A and B).
k. Composition of clones of different sizes within *NGFR*-high cluster 4 for both trametinib- and vemurafenib-treated splits.
l. A pie chart to demonstrate that of all the clones (barcodes) present in the trametinib-treated split in cluster 4, 20.7% were also present in the vemurafenib-treated split.
m. A cumulative density contour plot capturing the types of fate switches that the *NGFR*-high cluster 4 clones from the vemurafenib-treated split adopt in the trametinib-treated split.
n. Two representative examples of UMAP regions where twins from the *NGFR*-high cluster 4 in trametinib-treated split adopt in the vemurafenib-treated split.
o. UMAP for combined vemurafenib and trametinib treatment conditions recolored for each cell by its expression of the gene *VCAM1,* which is enriched in cluster 6.

p. Painting of singletons and colonies onto the UMAP for the *NGFR*-high cluster 4, colored by the condition, showing a relative enrichment of cells from trametinib as compared to vemurafenib. This panel also demonstrates that both singletons and colonies occupy cluster 4 from each of the two conditions.
q. We performed antibody stainings for NGFR on colonies emerging from treatment of the same number of starting melanoma cells with either vemurafenib or trametinib. Consistent with FateMap, we found an increased number of NGFR-positive resistant cells in trametinib treated cells as compared to the vemurafenib treatment.
r. UMAP split by each drug condition (trametinib (8,569 cells) or vemurafenib and trametinib (7,023 cells)), with colors representing clusters determined using Seurat's FindClusters command at a resolution of 0.5 (i.e. "Seurat clusters, resolution = 0.5").
s. UMAP recolored for combined resistant cells from trametinib (light blue) and vemurafenib and trametinib (dark blue). The cells from two conditions are interspersed into each other on the UMAP.

Extended Data Figure 10: Inhibition of histone methyltransferase DOT1L results in the emergence of additional resistant proliferative clones and a reduction in singletons.

a. For each barcode identified by sequencing, we plotted its abundance in corresponding splits A (DMSO control) and B (DOT1L inhibition). Those present in both control and DOT1L splits are colored in dark blue, and those present only in either A (control) and B (DOT1L) are colored in cyan. Those present in both (dark blue; 171) exhibited a strong correlation, suggesting that their ability to survive and become resistant is invariant of drug dose. For those present only in either (cyan), we found them to be much more abundant in DOT1L (B, 43 barcodes) than DMSO control (A, 7 barcodes), suggesting that new barcodes, otherwise unable to survive in the control condition, become drug-resistant in the DOT1L inhibited condition. A total of one biological replicate.
b. (left) Combined resistant cells in the control (9,343 cells) and DOT1L (7,044 cells) conditions obtained from UMAP applied to the first 50 principal components. Cells are colored by clusters determined using Seurat's FindClusters command("Seurat clusters, resolution = 0.8"). (right) UMAP is split by each condition.
c. UMAP where the resistant cells are colored by the associated condition (control vs DOT1L). The arrow represents the UMAP region present predominantly in the control region and missing from the DOT1L-associated UMAP region.
d. Quantification of singletons and colonies showed that while the number of resistant colonies is higher in DOT1L, it is accompanied by a reduced number of singletons cells compared to control.
e. Painting of singletons and colonies onto the UMAP, colored by the condition, demonstrated that singletons largely belong to the control condition and are present predominantly in cluster 2 (*MLANA*-high). Colonies are dispersed more across the UMAP with no particular region enriched for either condition.
f. Imaging of the nuclei (DAPI-stained) of resistant colonies emerging from vemurafenib treatment of WM989 A6-G3 cells, either for control or cells lacking DOT1L.
g. Quantification of the total number of colonies and singletons from each fate type across n=3 biological replicates demonstrated a relative increase (3.65-fold; n=3 biological replicates) in total colonies and reduction in total singletons in the DOT1L and control conditions, respectively.

h. UMAP is recolored for each cell by its expression for the gene *MLANA*, a marker for cluster 2, which is relatively enriched in control (as shown with an arrow).
i. A pie chart to demonstrate that of all the clones (barcodes) present in the control condition split, only 3.1% were also present in the DOT1L inhibitor pretreatment split.
j. Two representative examples of UMAP regions where twins from the *MLAN*A-high cluster in the control condition go in the DOT1L condition. A cumulative density contour plot capturing the types of fate switches that *MLANA*-high cluster clones from control adopt in the DOT1L inhibitor-pretreated condition.
k. A cumulative density contour plot capturing the types of fate switches that the *MLANA*-high cluster 2 clones from the control condition split adopt in the DOT1L inhibitor pretreatment split.
l. Distribution of cells across clusters for control (top) and DOT1L inhibitor-pretreated (bottom) conditions for clone size>2.

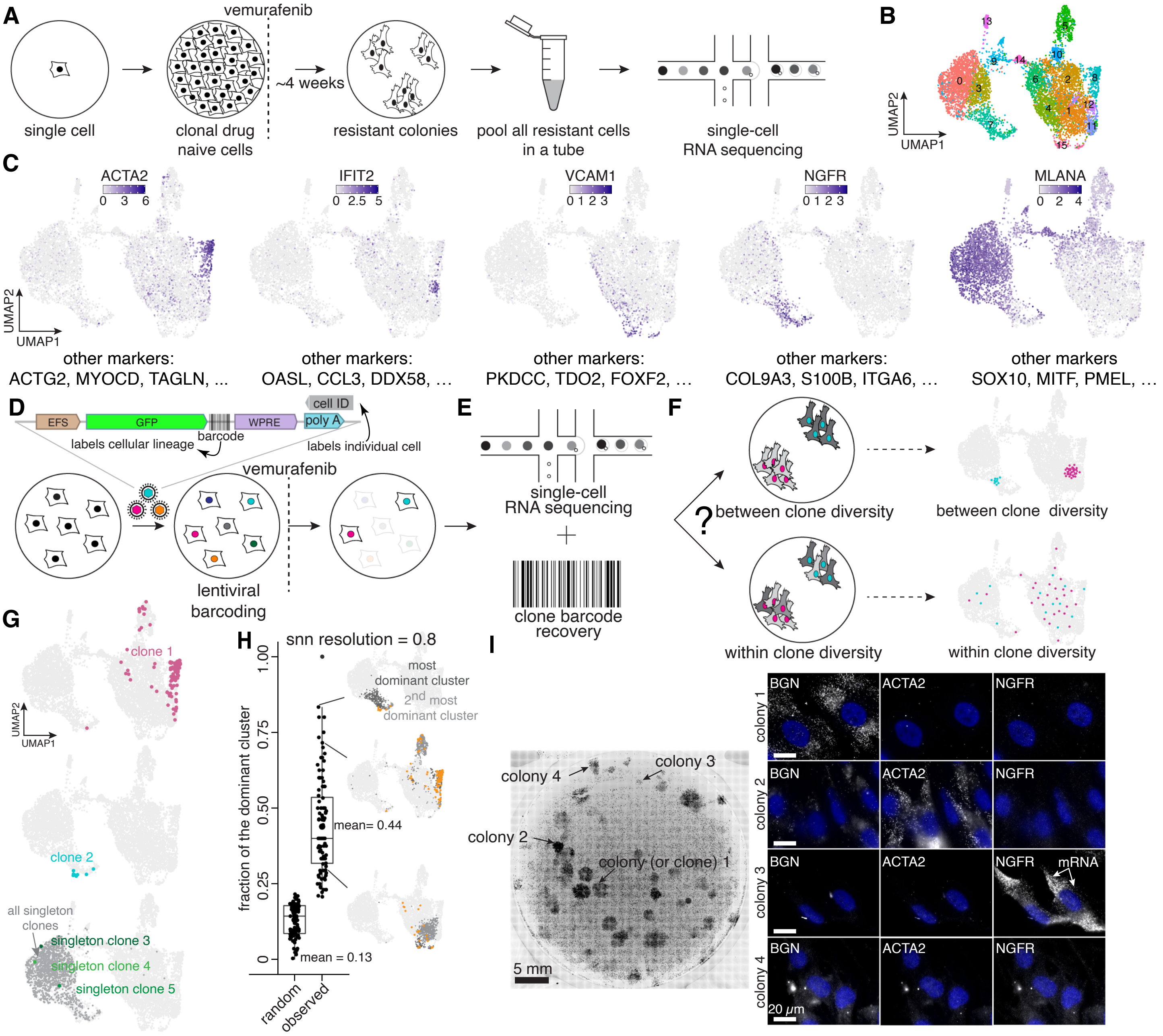
A
vemurafenib
single cell
clonal drug naive cells
~4 weeks
resistant colonies
pool all resistant cells in a tube
single-cell RNA sequencing
B
UMAP2
UMAP1
0
1
2
3
4
5
6
7
8
9
10
11
12
13
14
15
C
ACTA2
0 3 6
IFIT2
0 2.5 5
VCAM1
0 1 2 3
NGFR
0 1 2 3
MLANA
0 2 4
UMAP2
UMAP1
other markers:
ACTG2, MYOCD, TAGLN, ...
other markers:
OASL, CCL3, DDX58, …
other markers:
PKDCC, TDO2, FOXF2, …
other markers:
COL9A3, S100B, ITGA6, …
other markers
SOX10, MITF, PMEL, …
D
EFS
GFP
barcode
WPRE
cell ID
poly A
labels cellular lineage
labels individual cell
vemurafenib
lentiviral barcoding
E
single-cell RNA sequencing
+
clone barcode recovery
F
?
between clone diversity
between clone diversity
within clone diversity
within clone diversity
G
clone 1
UMAP2
UMAP1
clone 2
all singleton clones
singleton clone 3
singleton clone 4
singleton clone 5
H
snn resolution = 0.8
fraction of the dominant cluster
0
0.25
0.50
0.75
1.00
most dominant cluster
2nd most dominant cluster
mean= 0.44
mean = 0.13
random
observed
I
colony 4
colony 3
colony 2
colony (or clone) 1
5 mm
BGN
ACTA2
NGFR
colony 1
colony 2
colony 3
colony 4
mRNA
20 μm

Figure 1

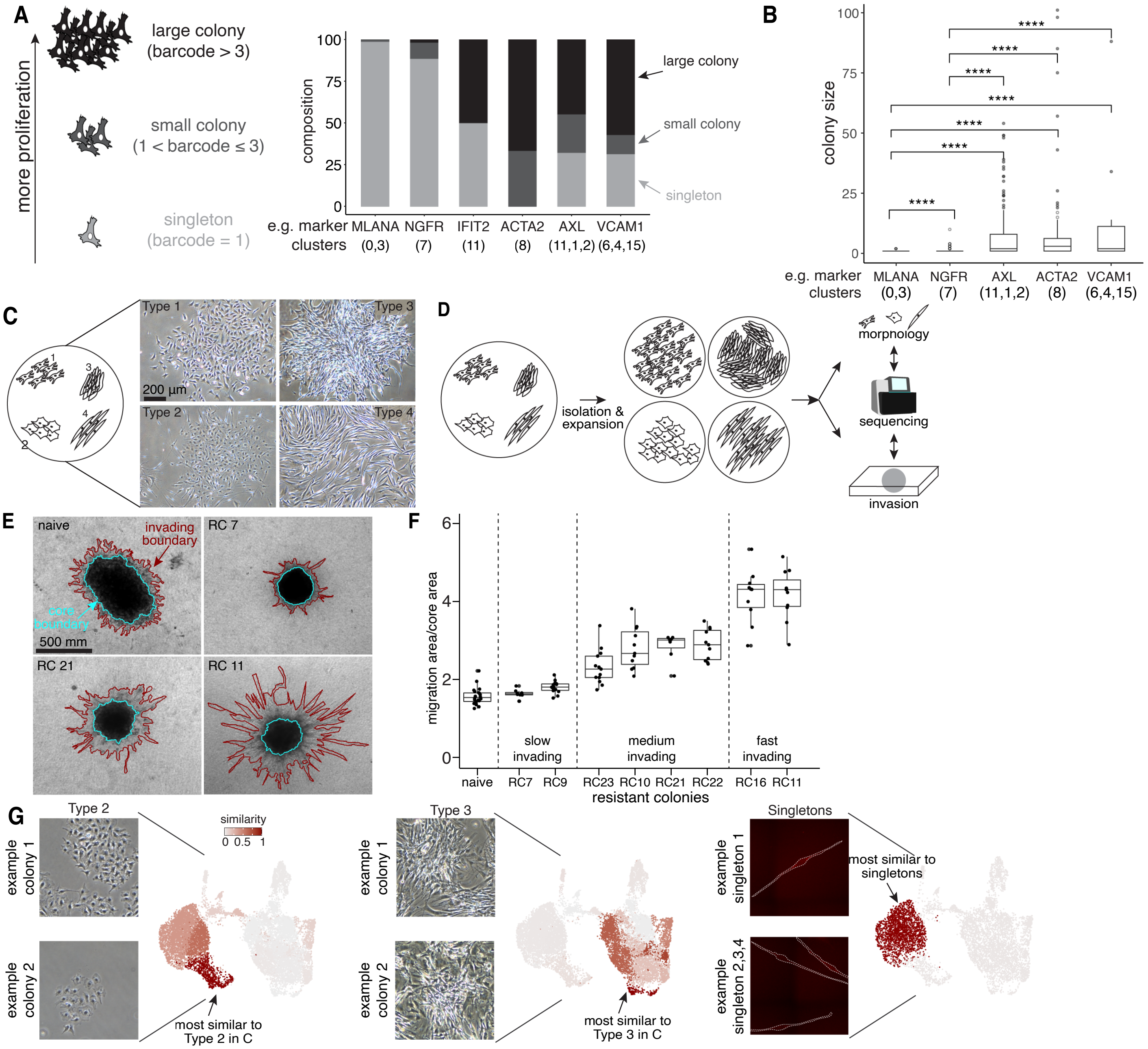
A
more proliferation
large colony
(barcode > 3)
small colony
(1 < barcode ≤ 3)
singleton
(barcode = 1)
composition
100
75
50
25
0
e.g. marker
clusters
MLANA (0,3)
NGFR (7)
IFIT2 (11)
ACTA2 (8)
AXL (11,1,2)
VCAM1 (6,4,15)
large colony
small colony
singleton
B
colony size
100
75
50
25
0
****
e.g. marker
clusters
MLANA (0,3)
NGFR (7)
AXL (11,1,2)
ACTA2 (8)
VCAM1 (6,4,15)
C
1
2
3
4
Type 1
Type 2
Type 3
Type 4
200 µm
D
isolation &
expansion
morphology
sequencing
invasion
E
naive
invading
boundary
core
boundary
500 mm
RC 7
RC 21
RC 11
F
migration area/core area
6
4
2
0
slow
invading
medium
invading
fast
invading
naive
RC7
RC9
RC23
RC10
RC21
RC22
RC16
RC11
resistant colonies
G
Type 2
example
colony 1
example
colony 2
similarity
0 0.5 1
most similar to
Type 2 in C
Type 3
example
colony 1
example
colony 2
most similar to
Type 3 in C
Singletons
example
singleton 1
example
singleton 2,3,4
most similar to
singletons

Figure 2

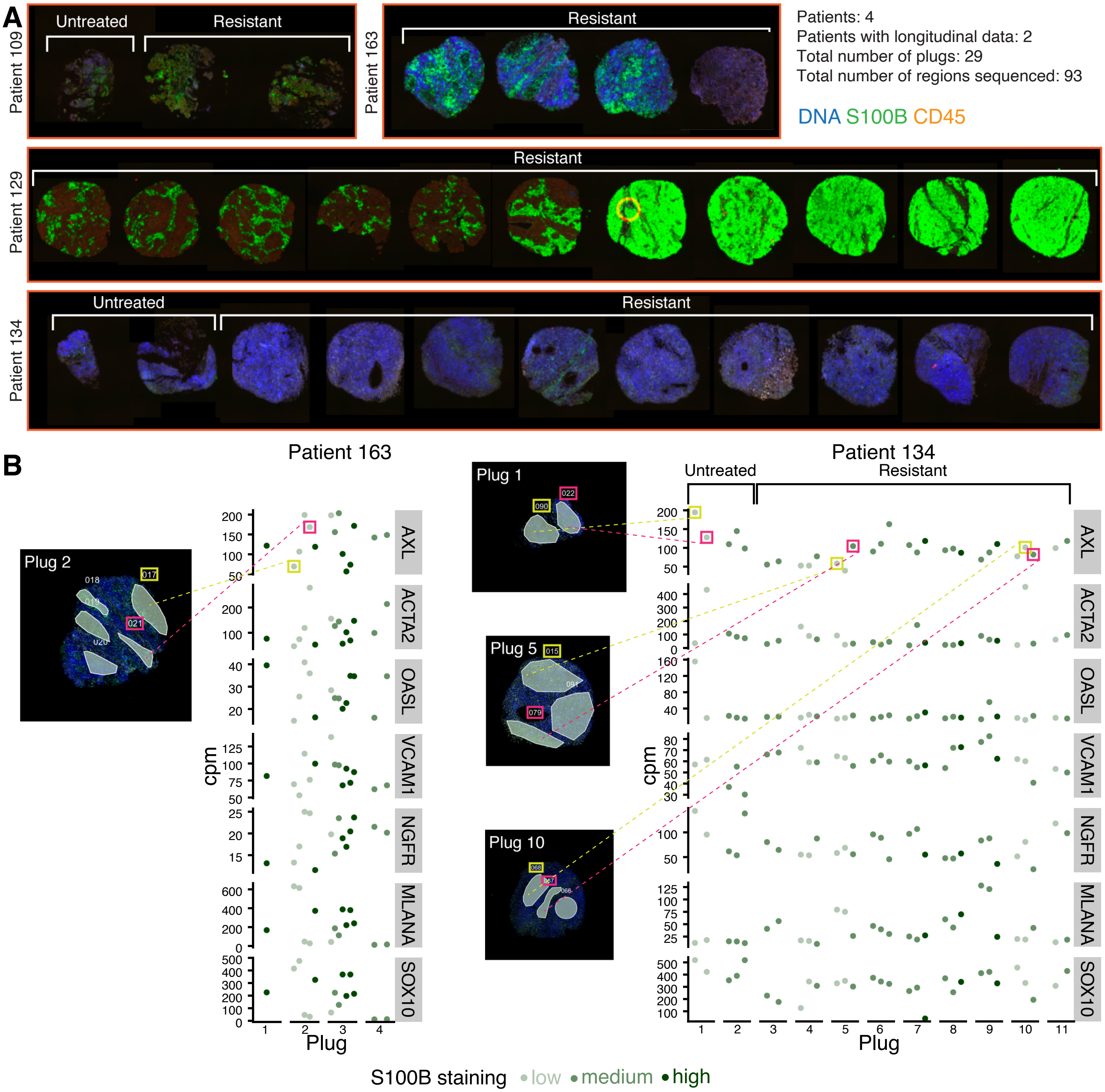
A
Patient 109
Untreated
Resistant
Patient 163
Resistant
Patients: 4
Patients with longitudinal data: 2
Total number of plugs: 29
Total number of regions sequenced: 93
DNA S100B CD45
Patient 129
Resistant
Patient 134
Untreated
Resistant
B
Patient 163
Plug 2
018
019
017
021
020
cpm
AXL
ACTA2
OASL
VCAM1
NGFR
MLANA
SOX10
1
2
3
4
Plug
Plug 1
090
022
Plug 5
015
091
079
Plug 10
068
067
066
Patient 134
Untreated
Resistant
cpm
AXL
ACTA2
OASL
VCAM1
NGFR
MLANA
SOX10
1
2
3
4
5
6
7
8
9
10
11
Plug
S100B staining ● low ● medium ● high

Figure 3

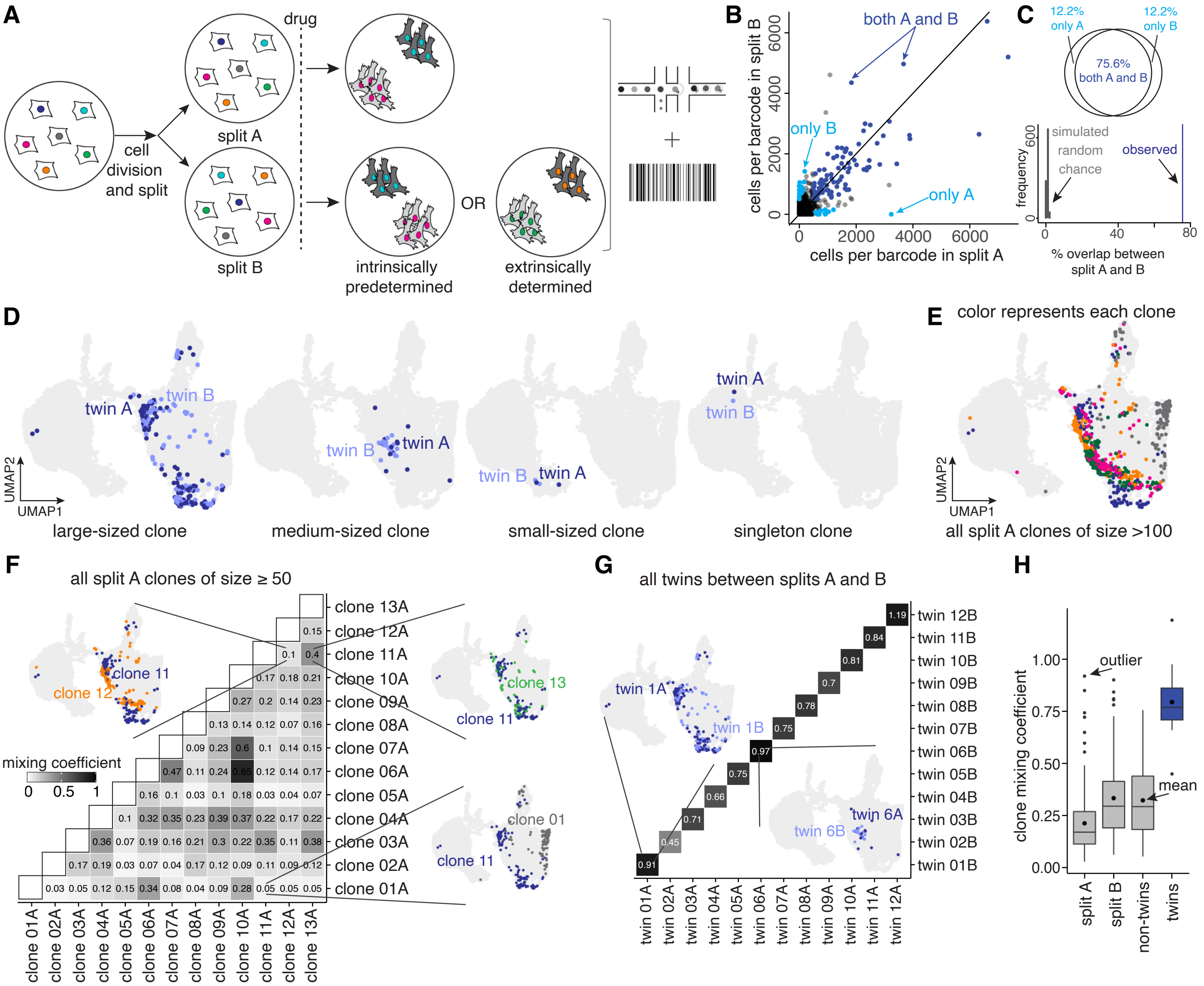
A
drug
cell division and split
split A
split B
intrinsically predetermined
OR
extrinsically determined
+
B
both A and B
only B
only A
cells per barcode in split B
cells per barcode in split A
0
2000
4000
6000
C
12.2% only A
12.2% only B
75.6% both A and B
simulated random chance
observed
frequency
600
0
40
80
% overlap between split A and B
D
twin A
twin B
UMAP2
UMAP1
large-sized clone
medium-sized clone
small-sized clone
singleton clone
E
color represents each clone
all split A clones of size >100
F
all split A clones of size ≥ 50
clone 11
clone 12
clone 13
clone 01
mixing coefficient
0
0.5
1
clone 13A
clone 12A 0.15
clone 11A 0.1 0.4
clone 10A 0.17 0.18 0.21
clone 09A 0.27 0.2 0.14 0.23
clone 08A 0.13 0.14 0.12 0.07 0.16
clone 07A 0.09 0.23 0.6 0.1 0.14 0.15
clone 06A 0.47 0.11 0.24 0.85 0.12 0.14 0.17
clone 05A 0.16 0.1 0.03 0.1 0.18 0.03 0.04 0.07
clone 04A 0.1 0.32 0.35 0.23 0.39 0.37 0.22 0.17 0.22
clone 03A 0.36 0.07 0.19 0.16 0.21 0.3 0.22 0.35 0.11 0.38
clone 02A 0.17 0.19 0.03 0.07 0.04 0.17 0.12 0.09 0.11 0.09 0.12
clone 01A 0.03 0.05 0.12 0.15 0.34 0.08 0.04 0.09 0.28 0.05 0.05 0.05
clone 01A
clone 02A
clone 03A
clone 04A
clone 05A
clone 06A
clone 07A
clone 08A
clone 09A
clone 10A
clone 11A
clone 12A
clone 13A
G
all twins between splits A and B
twin 1A
twin 1B
twin 6A
twin 6B
twin 12B 1.19
twin 11B 0.84
twin 10B 0.81
twin 09B 0.7
twin 08B 0.78
twin 07B 0.75
twin 06B 0.97
twin 05B 0.75
twin 04B 0.66
twin 03B 0.71
twin 02B 0.45
twin 01B 0.91
twin 01A
twin 02A
twin 03A
twin 04A
twin 05A
twin 06A
twin 07A
twin 08A
twin 09A
twin 10A
twin 11A
twin 12A
H
clone mixing coefficient
1.00
0.75
0.50
0.25
0.00
outlier
mean
split A
split B
non-twins
twins

Figure 4

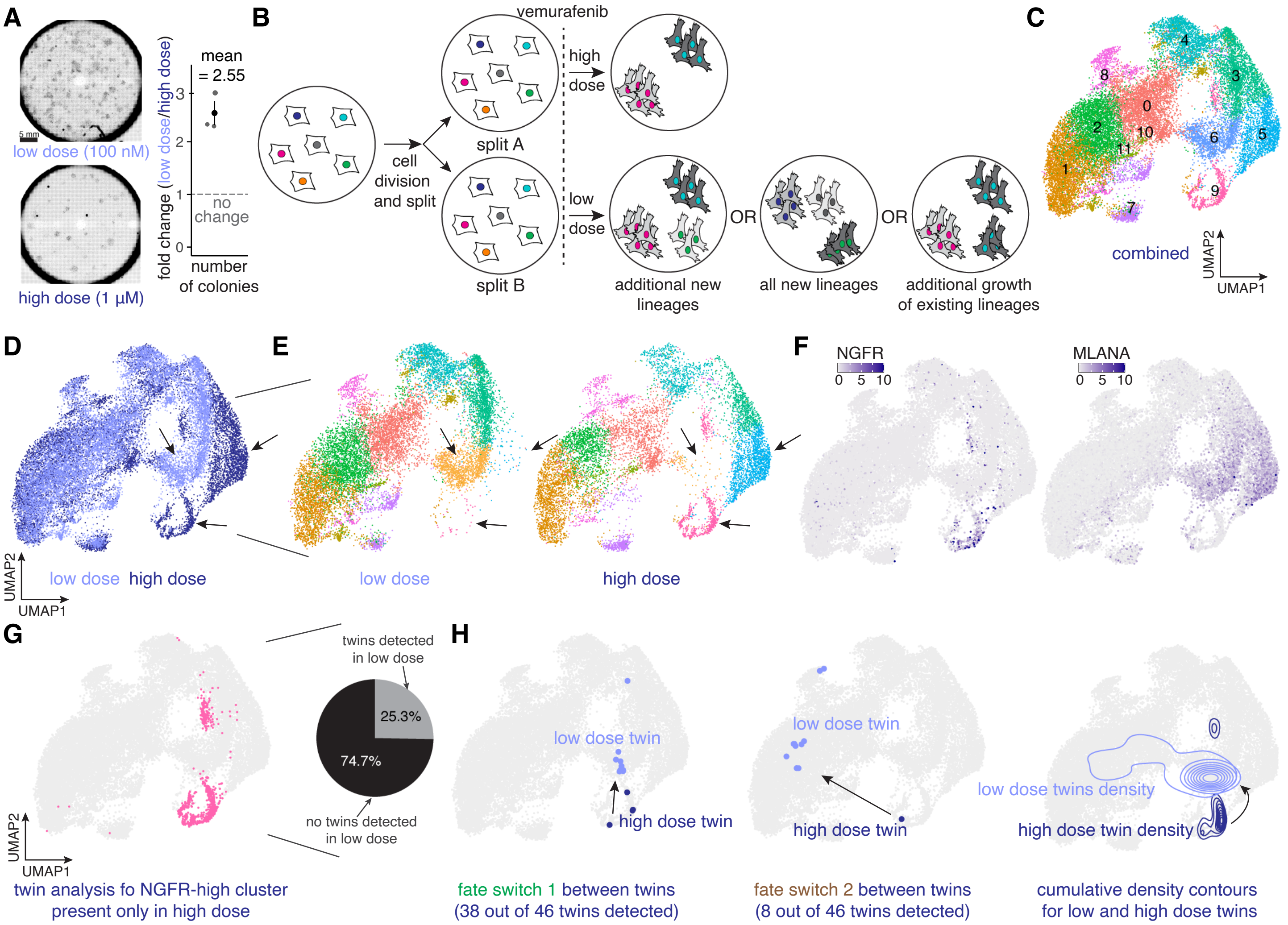
A
5 mm
low dose (100 nM)
high dose (1 µM)
fold change (low dose/high dose)
mean
= 2.55
0
1
2
3
no
change
number
of colonies
B
vemurafenib
cell
division
and split
split A
split B
high
dose
low
dose
additional new
lineages
OR
all new lineages
OR
additional growth
of existing lineages
C
0
1
2
3
4
5
6
7
8
9
10
11
combined
UMAP2
UMAP1
D
low dose
high dose
UMAP2
UMAP1
E
low dose
high dose
F
NGFR
0 5 10
MLANA
0 5 10
G
twins detected
in low dose
25.3%
74.7%
no twins detected
in low dose
UMAP2
UMAP1
twin analysis fo NGFR-high cluster
present only in high dose
H
low dose twin
high dose twin
fate switch 1 between twins
(38 out of 46 twins detected)
low dose twin
high dose twin
fate switch 2 between twins
(8 out of 46 twins detected)
low dose twins density
high dose twin density
cumulative density contours
for low and high dose twins

Figure 5